



Publication Year	2019
Acceptance in OA@INAF	2021-01-12T08:25:11Z
Title	The Gaia ultracool dwarf sample - II. Structure at the end of the main sequence
Authors	SMART, Richard Laurence; Marocco, F.; Sarro, L. M.; Barrado, D.; Beamín, J. C.; et al.
DOI	10.1093/mnras/stz678
Handle	http://hdl.handle.net/20.500.12386/29679
Journal	MONTHLY NOTICES OF THE ROYAL ASTRONOMICAL SOCIETY
Number	485

The *Gaia* ultracool dwarf sample – II. Structure at the end of the main sequence

R. L. Smart^{1,2★}, F. Marocco,³ L. M. Sarro,⁴ D. Barrado,⁵ J. C. Beamín,⁶
J. A. Caballero⁵ and H. R. A. Jones²

¹*Istituto Nazionale di Astrofisica, Osservatorio Astrofisico di Torino, Strada Osservatorio 20, I-10025 Pino Torinese, Italy*

²*School of Physics, Astronomy and Mathematics, University of Hertfordshire, College Lane, Hatfield AL10 9AB, UK*

³*Jet Propulsion Laboratory, California Institute of Technology, 4800 Oak Grove Dr., Pasadena, CA 91109, USA*

⁴*Departamento de Inteligencia Artificial, ETSI Informática, UNED, Juan del Rosal, E-16 28040 Madrid, Spain*

⁵*Centro de Astrobiología (INTA-CSIC), ESAC campus, Camino Bajo del Castillo s/n, E-28692 Villanueva de la Cañada, Madrid, Spain.*

⁶*Centro de comunicación de las ciencias, Universidad Autónoma de Chile, Santiago, Chile*

Accepted 2019 March 6. Received 2019 March 6; in original form 2018 September 13

ABSTRACT

We identify and investigate known late M, L, and T dwarfs in the *Gaia* second data release. This sample is being used as a training set in the *Gaia* data processing chain of the ultracool dwarfs work package. We find 695 objects in the optical spectral range M8–T6 with accurate *Gaia* coordinates, proper motions, and parallaxes which we combine with published spectral types and photometry from large area optical and infrared sky surveys. We find that 100 objects are in 47 multiple systems, of which 27 systems are published and 20 are new. These will be useful benchmark systems and we discuss the requirements to produce a complete catalogue of multiple systems with an ultracool dwarf component. We examine the magnitudes in the *Gaia* passbands and find that the G_{BP} magnitudes are unreliable and should not be used for these objects. We examine progressively redder colour–magnitude diagrams and see a notable increase in the main-sequence scatter and a bivariate main sequence for old and young objects. We provide an absolute magnitude – spectral subtype calibration for G and G_{RP} passbands along with linear fits over the range M8–L8 for other passbands.

Key words: binaries: visual – brown dwarfs – Hertzsprung–Russell and colour–magnitude diagrams – stars: late-type – solar neighbourhood.

1 INTRODUCTION

The *Gaia* second data release (hereafter *Gaia* DR2; Gaia Collaboration 2018a) was made on 2018 April 25 and contains parallaxes, proper motions, and magnitudes for over one billion objects. The main astrometric observations use a large optical passband called the G band, and the completeness magnitude goal of this mission in this band is 20.7 mag (Gaia Collaboration 2016). We are interested in ultracool dwarfs (hereafter UCDs), defined as objects with a spectral type later than M7. UCDs are intrinsically very faint in the optical and, therefore, only limited numbers will be observable by *Gaia*. In particular, we expect there to be around a 1000 L dwarfs and only a few T dwarfs (Haywood & Jordi 2002; Sarro et al. 2013; Smart 2014; Smart et al. 2017).

While this sample is relatively limited in numbers, the availability of all-sky uniformly derived parallaxes provides a volume-limited sample that is very useful for a number of astrophysical problems.

Gaia UCDs include objects with masses that straddle the stellar–substellar transition, and therefore help us define the observational boundary between hydrogen-burning stars and degenerate brown dwarfs (see e.g. Chabrier et al. 2009; Burrows, Heng & Nampaisarn 2011). The final volume-limited sample will be used to model the stellar–substellar mass function (Allen et al. 2005) and luminosity function (Cruz et al. 2007), removing incompleteness and observational biases (e.g. Malmquist, Eddington, and Lutz–Kelker effects) that plague current measurements of this fundamental observable (see e.g. Kirkpatrick et al. 2012; Marocco et al. 2015, and references therein).

The *Gaia* astrometry and photometry will provide robust measurements of luminosity. The *Gaia* data set will aid the modelling of the atmospheres of low-mass objects by providing a cohort of new benchmark systems, such as companions to main-sequence stars (Marocco et al. 2017; Montes et al. 2018) and members of young moving groups (e.g. Gagné et al. 2015). L dwarfs are analogues for understanding planetary atmospheres (Faherty et al. 2016) and, once we calibrate a cooling curve (e.g. by studying L dwarf companions to white dwarfs; Day-Jones et al. 2011),

* E-mail: richard.smart@inaf.it

their ubiquity will make them promising Galactic chronometers (Burgasser 2009; Soderblom 2010).

A first step in identifying *Gaia* L and T (hereafter LT) dwarfs was carried out in Smart et al. (2017, hereafter Paper 1), matching known LT dwarfs to the first *Gaia* data release (Gaia Collaboration 2016), which contained accurate positions and *G* magnitudes for 1.14 billion objects. This cross-match resulted in 321 LT dwarfs with *Gaia* *G* magnitudes and positions. This catalogue makes up the cool part of the *Gaia* ultracool dwarf sample (hereafter GUCDS), which is being used as a training set in Coordination Unit 8 of the *Gaia* Data Processing and Analysis Consortium pipeline.¹ In addition, Gaia Collaboration (2018b) cross-matched the input catalogue from Paper 1 with *Gaia* DR2 and external catalogues such as 2MASS (Skrutskie et al. 2006). This exercise provided 601 LT dwarfs, including 527 fully characterized objects. Here, we build on this legacy and carry out a more comprehensive analysis.

In this paper we concentrate on the LT dwarfs that are in the *Gaia* DR2. In Section 2 we describe the input catalogue of LT dwarfs used to search the *Gaia* DR2, the cleaning carried out, and the production of the LT part of the GUCDS catalogue. In Section 3 we look at LT dwarfs that are in binary systems with other objects in the *Gaia* DR2. In Section 4 we examine this catalogue in absolute magnitude, colour, and spectroscopic space. In the last section we give conclusions and future plans.

2 THE COMPARISON CATALOGUES

2.1 The *Gaia* DR2 selection

Each of the 1332 million *Gaia* DR2 sources with full astrometric solutions are the result of individual five-parameter fits to their epoch positions. It is inevitable that some of these fits produce physically nonsensical solutions with large negative parallaxes being the most obvious examples. The solutions with large positive parallaxes that appear to be nearby objects represent the tail of the 10^9 solutions distribution and is, in a relative sense, significantly impacted by objects being scattered into that solution space. Indeed, if one orders *Gaia* DR2 by parallax, Proxima Centauri, the closest object to the Sun, would be ranked 61st. If we consider objects with parallaxes greater than 200 mas (i.e. distance $d < 5$ pc), there are 792 of them in the *Gaia* DR2. However, only 38 have a parallax in SIMBAD (Wenger et al. 2000) that is greater than 200 mas. There are also 34 of the 792 objects that match to SIMBAD entries but have parallaxes or photometric distances that place them at distances greater than 5 pc. While there is a remote possibility that some of the new objects with parallaxes greater than 200 mas in the *Gaia* DR2 are really within 5 pc, the majority, if not all, of the remaining 754 solutions are incorrect.

In Lindegren et al. (2018, their appendix C) they convincingly argued that many of these bad solutions are due to mismatches of the observations. They showed, as it would be expected if this is the dominant reason, that the number of objects with large negative parallaxes is approximately equal to the number of sources with large spurious positive parallaxes. They also provided a number of quality cuts that would reduce the contamination at a small cost to the identification of real objects. However, as our final goal is to make a complete census of all UCDs in the *Gaia* data set, we want our training set to include also objects with low-quality astrometry so we do not apply those cuts. In addition, the *Gaia* DR2 is missing

astrometric solutions for prominent nearby bright LT dwarfs, e.g. *WISE* J1049–5319A, (Luhman 2013) and ϵ Indi B ab (Scholz et al. 2003), probably because these are binary systems with large orbital motions and their solutions did not meet the quality thresholds for inclusion in the *Gaia* DR2.

Since the majority of large parallaxes are unreliable and some of the nearest objects are missing, it is premature to attempt to find all UCDs to the *Gaia* magnitude limit and, therefore, we concentrate on developing criteria for a robust selection procedure in the future. The first step in developing such criteria is the identification of known UCDs that we can use as a training set. In Paper 1 we showed that the most distant single L0 that we expected to see in *Gaia* is at 80 pc. There are unresolved binary L dwarf systems outside the 100 pc limit that have a combined magnitude greater than the *Gaia* DR2 limit. There are also very young L dwarfs that have very bright intrinsic magnitudes for their spectral type and these may enter the *Gaia* DR2 even though they are at a distance greater than 100 pc. For example some of the L dwarfs identified in the Upper Scorpius OB association (see Lodieu et al. 2008, and reference therein) at a distance of 145 ± 2 pc (de Zeeuw et al. 1999) with an age of 5 Myr (Preibisch & Zinnecker 1999) have predicted *Gaia* apparent magnitudes $G < 20$ mag from Paper 1. However, the vast majority of LT dwarfs seen by *Gaia* are within 80 pc, so we start by selecting all objects from the *Gaia* DR2 with a parallax greater than 10 mas, e.g. a distance limit of 100 pc, which results in 700 055 sources.

2.2 The M, L, T, or Y catalogue

The initial list of known UCDs was the input catalogue from Paper 1 of 1885 objects with M, L, T, or Y spectral classification. To this we added the photometrically identified LT dwarfs from Skrzypek, Warren & Faherty (2016) and a few other recent discoveries (e.g. Marocco et al. 2017; Scholz & Bell 2018; Smith et al. 2018). The current list contains 3093 UCDs ranging from M8 to Y2 dwarfs. The M dwarfs were retained to facilitate differentiation of the spectral types in the magnitude and colour space, as some objects are classed as M in optical spectra and L in infrared spectra and vice versa. Since this input catalogue is dominated by L and T dwarfs we refer to it as the LT catalogue (hereafter LTC).

For all objects we have collected photometry from the Two Micron All Sky Survey (2MASS; Skrutskie et al. 2006), the Panoramic Survey Telescope and Rapid Response System release 1 (PS1; Chambers et al. 2016), and the *Wide-field Infrared Survey Explorer* extension (AllWISE; Wright et al. 2010), providing up to 11 homogeneous magnitudes in passbands ranging from Gunn *g* to *WISE* W3. The *WISE* W4 band was not included as the number of objects with reliable magnitudes were very low.

We started by searching for any objects in the *Gaia* DR2 release that had a parallax larger than 10 mas and was within 20 arcsec of the LTC entry at the *Gaia* DR2 epoch. We choose 20 arcsec as not all entries have published proper motions, the epoch difference can be up to 20 yr, and typical proper motions are 500–1000 mas yr⁻¹. This resulted in 753 entries from *Gaia* DR2. For each entry we then propagated the *Gaia* DR2 position to the epoch of the LTC positions in the input catalogue using the *Gaia* DR2 proper motions.

2.3 Treatment of duplicate matches

Some multiple LTC dwarfs matched to the same *Gaia* DR2 source, e.g. J1416+1348A/J1416+1348B to 1227133699053734528 and J1207–3932A/J1207–3932B (TWA 27 A and B) to 3459372646830687104. These are known binary systems where

¹<https://www.cosmos.esa.int/web/gaia/coordination-units>.

both the primary and secondary are in our LTC and, the primary is observed by *Gaia* but the secondary is not. This maybe because the secondary is faint, e.g. J1416+1348B has an estimated $G = 23.9$, or the primary and secondary are very close and are not resolved in the *Gaia* DR2 e.g. TWA 27A/B have a separation of 0.7 arcsec (Chauvin et al. 2004). For these multiple LTC entry matches we assumed that the correct match was the brightest of the binary system.

In general the closest of multiple matches in the *Gaia* DR2 at the epoch of the LTC position is the correct one, but this may not be always the case. Using only unique matches we calibrated robust linear relations between the *Gaia* DR2 G magnitude and the optical spectral types for each LTC entry with external optical photometry, and the near-infrared (NIR) spectral types with external NIR photometry. Using these relations, we estimated an average magnitude G_{est} for all objects in the LTC (see Paper 1). There were 21 LTC entries with more than one *Gaia* DR2 object within 20 arcsec. In Table 1 we report for these objects the source identification number, `SOURCE_ID`, of the matched *Gaia* DR2 entries, the offset on the sky of the LTC position (generally 2MASS coordinates) and the *Gaia* DR2 entry, G magnitude, $G - G_{\text{est}}$ difference, parallax in milliarcseconds (hereafter mas), total proper motion in mas yr^{-1} and position angle of the proper motion in degrees.

In all cases the nearest positional match also has the smallest $G - G_{\text{est}}$, consistent with being the LT dwarf. Extra objects within 20 arcsec are in most cases the other component in known physical binary systems, as is evident when the ‘Discovery Name’ indicates the LT dwarf is the B component in a known system. To all these combinations we applied the binary test described in Section 5, and if a pair satisfies it – i.e. we consider the pair to be a physical system – we label it ‘Bin’ in the first column.

There are three matches that did not pass our binarity test: J0235–2331, J1442+6603A, and J1540+0102. Both J0235–2331 (GJ 1048 B) and J1442+6603 (G239-25B) are in known binary systems where the primary has been correctly identified in Table 1. These represent a failure of our binarity test; reasons for this could be that the orbital motion is significant so the proper motions are not within 10 percent, or simply bad solutions; we discuss this in Section 5. For J1540+0102, the nearby object 4416887712294719104 has a parallax that differs by more than 3σ , but it is at the limit and has consistent proper motions, so it warrants further consideration. Most binary systems are already noted in the literature except J1219+0154 and J2308+0629, which were first published in Skrzypek et al. (2016) and photometrically classified as single L dwarfs. Since this is quite a recent study, the entries have not received a significant amount of follow-up, so new candidate binary system discoveries are not unexpected. Systems of particular interest are discussed in Section 5.

2.4 Cleaning of matched objects

The majority (93 percent) of objects in the *Gaia* DR2 with $\varpi > 10$ mas have $\varpi/\sigma_{\varpi} > 5$. Since we are considering each object individually, for our selection purposes it is sufficient to use a simple distance given by the inverse of the parallax, $1/\varpi$ (Bailer-Jones 2015). Using this distance, we calculated an absolute magnitude in the G band, M_G . Considering the bulk of L0 dwarfs, we found that a conservative absolute magnitude limit for this spectral type is $M_G = 14.0$ mag. Among the remaining 732 matched objects, only 34 are brighter than this magnitude which we visually inspected. Often they were incorrect matches where the LTC entry is a companion in a binary system that was too faint for *Gaia*, so instead we matched to the bright component, e.g. the T7 dwarf GJ 229B was matched to its

M1 V primary GJ 229A. However, some were just close unrelated stars, e.g. J1119+0021 is a T4.5 that was too faint for *Gaia* but matched to the unrelated object UCAC4 452-049871. On individual inspection of the 34 sources, only J1207–3932A, J1610–0040, and J0133–6314 appeared to be correct matches to late-type M dwarfs, and all other matches were removed. J1047+4046 was also probably correctly matched, but to an M6.5, so we did not retain it as it is outside our M7 limit. The details of these three objects are included in Table 2.

This absolute magnitude test was not possible for Paper 1 because there were no parallaxes, required to calculate distance moduli. In *Gaia* Collaboration (2018b) they used the Paper 1 input catalogue and did not apply this cleaning, so the very bright ‘LT objects’ on the main sequence of their fig. 9(a) and the white dwarf track of their fig. 9(c) are matches of the bright primary star to the fainter LT companion in the Paper 1 input catalogue.

After removing the bright objects we found five objects with an offset from the predicted position and the *Gaia* DR2 position larger than 5 arcsec. We retained the first two (J1711+4028 and J2250+0808), listed in Table 2, as both the magnitude difference $G - G_{\text{est}}$ were not very large, and in a visual inspection of the region there did not appear to be any other nearby objects. For the other three objects (J1108+1535, J1928+2356, and J1456–2747) they have a large offset from the LTC predicted position (19.4, 19.6, and 19.9 arcsec, respectively) and a large $G - G_{\text{est}}$ mag difference (–0.8, –2.3, and –2.8 mag, respectively). We conclude that these are objects undetected by *Gaia* that have been matched to a nearby unrelated star. The target J1928+2356 has a $G_{\text{est}} = 20.182$ mag, nominally within the *Gaia* magnitude limit and may appear in later releases, but the other two have $G_{\text{est}} > 21.0$ mag, so they will probably not be detected.

2.5 The GUCDS catalogue

After cleaning the initial match, our final catalogue is made up of 695 objects in the spectral range M8–T6 with *Gaia* astrometry. In the top panel of Fig. 1 we show the distribution of the 543 objects with optical spectral classification and the 384 with infrared spectral classification. There were eight unresolved systems where we assumed, for the distributions in Fig. 1, the earliest of the two spectral types. For example, J0320–0446 has an infrared spectral type of ‘M8.5 + T5.’ (Burgasser et al. 2008); for the distribution we assumed a spectral type of M8.5. There were also 69 objects with just a photometric spectral type from Skrzypek et al. (2016) that are not included in these figures.

In the lower panel of Fig. 1 we show the G , G_{RP} , and G_{BP} magnitude distributions. All 695 entries have a G magnitude (as well as a proper motion and a parallax), as this is a requirement for inclusion in the *Gaia* DR2, and 660 UCDs have G_{BP} and G_{RP} magnitudes. In Table 3 we list the astrometry, spectroscopy, photometry, and other parameters for the catalogue that are used in the following sections. The full catalogue is available online here and we will refer to it as the GUCDScat.

2.6 Comparison of parallaxes with published results

In the GUCDScat 151 entries have previously published parallaxes. In Fig. 2 we plot the *Gaia* DR2 versus the published values. In Table 4 we have listed all objects with *Gaia* DR2 and published values that differ by more than 2.5 times the combined uncertainties. There is only one significant outlier, J1506+7027, which had a parallax estimated in Marsh et al. (2013) of 310 ± 42 mas using

Table 1. Input catalogue entries with multiple *Gaia* DR2 matches within 20 arcsec, where both objects are in the input catalogue of UCDS we include their names. Objects with ‘Bin’ in the first column are found to be physical binaries based on the test discussed in Section 5.

Short name	Discovery Name and Source_ID	Offset (arcsec)	G (mag)	$G - G_{est}$ (mag)	ϖ (mas)	μ_{tot} (mas yr $^{-1}$)	θ_{μ} ($^{\circ}$)
J0004–4044	GJ 1001 B	0.8	18.353	–0.4	82.1 ± 0.4	1641.6	155.9
Bin	4996141155411983744	18.4	11.500	–7.2	81.2 ± 0.1	1650.7	155.8
J0235–2331	GJ 1048 B	0.1	18.598	0.6	46.6 ± 0.3	97.0	77.5
	5125414998097353600	12.1	7.987	–10.1	47.1 ± 0.0	84.5	80.4
J0858+2710	2MASS 08583693+2710518	0.1	19.926	0.3	18.9 ± 1.3	221.4	155.9
Bin	692611481331037952	15.2	15.067	–4.6	17.9 ± 0.1	215.0	156.8
J1004+5022	G 196-3 B	0.2	20.170	0.3	44.4 ± 0.8	250.0	213.5
Bin	824017070904063104	15.9	10.612	–9.3	45.9 ± 0.0	246.8	214.9
J1004–3335	2MASSWJ1004392–333518	0.3	19.615	0.3	53.3 ± 0.6	495.1	135.7
Bin	5458784415381054464	12.0	12.908	–6.5	53.5 ± 0.1	488.8	135.0
J1047+4046	LP213-067	4.4	15.183	–1.3	40.1 ± 0.1	299.9	263.7
J1047+4047	LP213-068	4.5	16.931	–0.7	38.9 ± 0.5	303.3	263.5
J1202+4204	2MASS 12025009+4204531	0.2	19.321	–0.5	31.5 ± 0.4	366.6	217.5
Bin	1537249785437526784	7.8	16.430	–3.4	31.6 ± 0.1	368.9	218.3
J1219+0154	ULAS J121932.54+015433.0	0.1	19.792	–0.6	18.9 ± 0.6	114.9	229.9
Bin	3700975728440669184	10.9	13.441	–6.9	19.8 ± 0.1	115.2	230.4
J1245+0156	ULAS J124531.54+015630.9	0.1	20.612	–0.5	13.5 ± 1.2	76.0	234.7
Bin	3702489721592680832	8.2	12.860	–8.3	13.2 ± 0.0	75.6	235.1
J1304+0907	2MASS 13043318+0907070	0.1	20.173	–0.4	18.2 ± 0.8	134.8	278.6
Bin	3734192764990097408	7.6	15.160	–5.4	17.8 ± 0.1	134.3	277.9
J1442+6603A	G 239-25 A	0.2	9.851	–2.3	91.5 ± 0.0	301.6	262.6
J1442+6603	G 239-25 B	0.2	15.302	–1.4	91.7 ± 0.2	338.5	274.3
J1520–4422	WDS J15200–4423A	0.4	18.293	–0.3	54.5 ± 0.2	736.7	238.6
J1520–4422B	WDS J15200–4423B	0.4	19.817	1.0	53.7 ± 0.6	753.4	238.6
J1540+0102	ULAS J154005.10+010208.7	0.0	19.851	–0.7	14.8 ± 0.6	51.7	253.1
	4416887712294719104	13.6	14.863	–5.6	17.0 ± 0.7	50.9	267.0
J1711+4028	G 203-50 B	5.5	20.232	–0.4	47.4 ± 0.7	263.5	72.4
Bin	1341903196663707904	8.7	14.233	–6.4	47.1 ± 0.1	265.5	72.0
J2200–3038A	DENIS-PJ220002.05–303832.9A	3.7	18.437	–0.3	25.4 ± 0.4	247.2	104.9
J2200–3038B	DENIS-PJ220002.05–303832.9B	0.1	19.042	–0.6	25.3 ± 0.5	253.7	105.6
J2308+0629	ULAS J230818.73+062951.4	0.1	18.059	–0.7	24.7 ± 0.3	118.5	162.3
Bin	2665079816223169664	3.8	13.467	–5.3	24.1 ± 0.1	119.8	160.5
J2322–6151	2MASS 23225299–6151275	0.0	20.682	0.3	23.2 ± 1.0	114.6	135.7
Bin	6487249243899899904	16.6	14.902	–5.5	23.6 ± 0.1	110.3	135.2

Table 2. *Top:* intrinsically bright ($M_G < 14.0$ mag) objects matched to LT objects sorted by absolute magnitude. *Bottom:* matches with offset > 5.0 arcsec sorted by separation.

Short name	Discovery name	Source_ID	Offset (arcsec)	G (mag)	G_{est} (mag)	M_G (mag)
J1207–3932A	TWA 27 A	3459372646830687104	0.02	17.408	17.450	13.363
J1610–0040	LSRJ 1610–0040	4406489184157821952	0.67	16.595	17.066	13.917
J0133–6314	SSSPM J0134–6315	4712132354155559040	0.05	18.206	19.652	13.919
J1711+4028	G 203-50 B	1341903196662424320	5.50	20.232	20.411	18.613
J2250+0808	BRLT 317	2713153831843361920	5.98	20.642	20.410	17.456

eight epochs over 2 yr from a combination of *WISE*, *WIRC*, and *Spitzer* compared to the *Gaia* DR2 value of 193.5 ± 0.9 mas. The photometric parallax for this object would be 187 mas based on the apparent magnitude–spectral type of the Dupuy & Liu (2012) calibration, consistent with the *Gaia* DR2 value. It is very difficult to successfully combine observations from different instruments in small field astrometry, and the *Gaia* DR2 solution does not give any indication of problem. Therefore we adopt the *Gaia* value.

The *Gaia* DR2 parallaxes have a median uncertainty of 0.4 mas while the published parallaxes have a median uncertainty of 1.5 mas.

For the objects with published parallaxes we calculated the ratio

$$r = \frac{\varpi_N - \varpi_P}{\sqrt{\sigma_N^2 + \sigma_P^2}}, \quad (1)$$

where ϖ is the parallax, σ the quoted uncertainties, and the subscripts N and P represent the new and published values, respectively. If the measures were unbiased and the uncertainties correct we would expect this ratio to follow a Gaussian distribution with a mean of zero and a standard deviation of unity. For the 151 common objects, after 3σ clipping, the mean is -0.02 and the standard

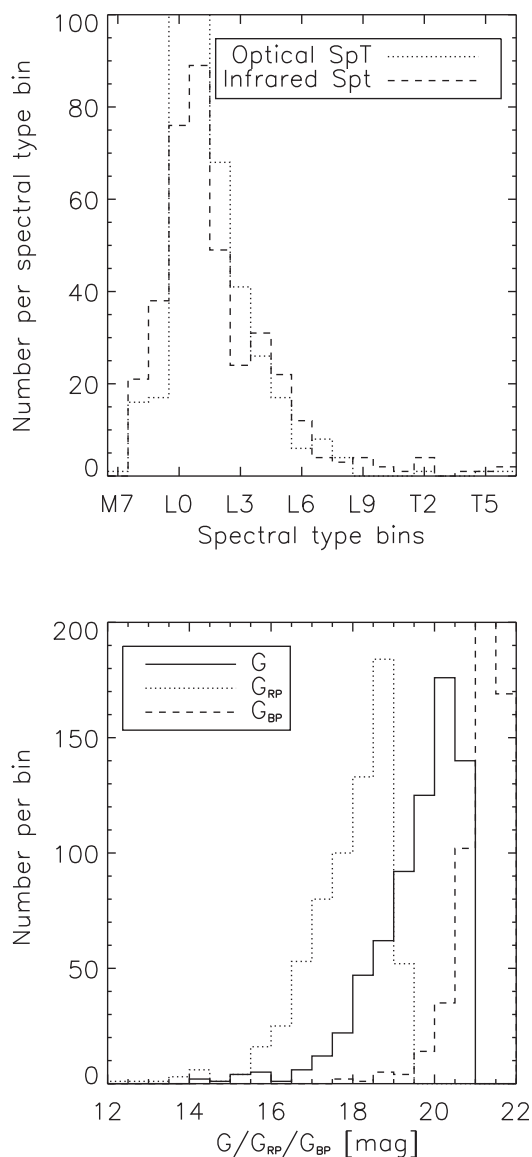


Figure 1. *Top:* distribution of optical and infrared spectral types in the GUCDS. Optical L0 and L1 bins have been truncated (they contain 202 and 105 objects, respectively). *Bottom:* distribution of *Gaia* magnitudes in the GUCDS.

deviation is 1.3. Applying the t -test at the 95 per cent level we find that the mean is not consistent with zero, i.e. $P(t) = 0.048$, while applying the F -test we find that the σ is significantly different from one, e.g. $P(F) = 2 \times 10^{-6}$. Since the σ of the ratio is greater than unity, the implication is that the uncertainties are underestimated. To reconcile the differences, the uncertainties of the published values would have to be increased by ~ 120 per cent, or those of *Gaia* by ~ 800 per cent. However, as is evident in Table 4, the source of published parallaxes is very heterogeneous, and the calculation of the errors are functions of the different program reduction routines. Hence to obtain applicable corrections the sample should be split into the contributing programs and then individually assessed. The *Gaia* DR2 will enable a characterization of the uncertainties of the different small field programs, and the *Gaia* parallaxes of the anonymous field stars used in the programs allow a precise estimate of the correction from relative to absolute parallax, which is one of the most unreliable steps in small field astrometry. In this way

Gaia will contribute to an improvement in the determination and characterization of parallaxes for objects that are fainter than its magnitude limit.

3 BINARY SYSTEMS

We searched for resolved binaries using the following criteria:

$$\begin{aligned} \rho &< 100\varpi, \\ \Delta\varpi &< \max[1.0, 3\sigma_\varpi], \\ \Delta\mu &< 0.1\mu, \\ \Delta\theta &< 15^\circ, \end{aligned} \quad (2)$$

where ρ is the separation on the sky in arcseconds, $\Delta\varpi$ is the difference of the GUCDS and candidate primary parallaxes, ϖ and σ_ϖ are the parallax and error of the GUCDS object, $\Delta\mu$ is the difference of the total proper motions, and $\Delta\theta$ is the difference of the position angles. The chosen ρ criterion is equivalent to 100 000 au, which is a conservative upper limit for a projected physical separation (s). This will meet the binding energy criterion of $|U_g^*| = GM_1M_2/s > 10^{33} J$ as developed by Caballero (2009) for a $0.1 + 2 M_\odot$ system (see also Dhital et al. 2010). The $\Delta\varpi$ criterion is based on a consideration of the errors, standard 3σ criterion or 1.0 mas, to allow for solutions that had unrealistically low errors. For the modulus and position angles of the proper motion, criteria based on the errors would remove nearby objects with significant orbital motion, hence we simply choose hard criteria of ~ 10 per cent in both parameters. This is large enough to accommodate most orbital motion, but small enough to avoid false positives. As discussed in Section 2.3 two secondaries in known wide binaries are missed by our criteria – J0235–2331 (GJ 1048 B) and J1442+6603 (G239-25B). We believe that in both cases the orbital motion accounts for a > 10 per cent discrepancy in the proper motion criteria.

There are 100 objects in 47 multiple systems including at least one of our GUCDS objects. We compared this list to a combination of the binary lists from the following publications: Mason et al. (2001), Deacon et al. (2014), De Rosa et al. (2014), Dhital et al. (2015), Gauza et al. (2015), Smith et al. (2015), Scholz (2016), Kirkpatrick et al. (2016), Gálvez-Ortiz et al. (2017), Deacon et al. (2017), and we found that 27 are known systems and 20 are new systems. We found two systems, WDS J15200–4423AB and DENIS-P J220002.05–303832.9AB, that were known spectroscopic binaries that *Gaia* resolves. In Table 5 we list systems that are particularly worthy of discussion. Several of them include primaries with no previous discussion in the literature, and are therefore identified with their *Gaia* ID.

(i) SDSS J12451496+1204423 (Zhang et al. 2010) is found to be a wide companion ($s \geq 7900$ au) to the DA white dwarf SDSS J124520.60+120531.3 (Kleinman et al. 2013). L dwarf + white dwarf non-interacting systems are precious benchmarks, since the white dwarf can provide accurate age constraints (see e.g. Day-Jones et al. 2011).

(ii) 2MASS J21265040–8140293 was identified by Deacon, Schlieder & Murphy (2016) as a companion to the young M dwarf TYC 9486-927-1. Analysis of the primary’s spectrum performed by Deacon et al. (2016) revealed Li $\lambda 6708 \text{ \AA}$ absorption consistent with an age range of 10–45 Myr, implying a mass range of $11.6\text{--}15 M_{\text{Jup}}$ for the secondary. With a projected separation of ~ 7400 au, 2MASS J21265040–8140293 is the widest orbit planetary-mass object known (Caballero 2018).

Table 3. Content of the GUCDScat with J1807+5015 as an example.

Parameter	Format	Unit	Comment	Example
SHORTNAME	a12	–	Short name used in text of paper	J1807+5015
RA	f13.9	deg	Right ascension (eq. J2000, ep. 2015)	271.816572024
Dec.	f13.9	deg	Declination (eq. J2000, ep. 2015)	50.258197767
DISCOVERYNAME	a25	–	Common discovery name	2MASSJ1807159 + 501531
DISCOVERYREFNAME	a19	–	Discovery reference	2003AJ....126.2421C
SOURCE_ID	i20	–	<i>Gaia</i> DR2 source ID	2123161836615550848
DISTARCSEC	f6.2	–	Distance DR2 to catalogue position	0.14
MULTIPLEFLAGNAME	a10	–	Multiple code VB/UR/MG	–
MULTIPLEFLAGREFNAME	a19	–	Multiple code reference BibCodes	–
SPTOPTNAME	a10	–	Optical spectral type	L1.5
SPTOPTREFNAME	a19	–	Optical spectral type BibCode	2003AJ....126.2421C
SPTNIRNAME	a10	–	NIR spectral type	L1
SPTNIRREFNAME	a19	–	NIR spectral type BibCode	2003IAUS..211..197W
SPTPHONAME	a10	–	Photometric spectral type	–
SPTPHOREFNAME	a19	–	Photometric spectral type BibCode	–
LIT_PARALLAX	f10.3	mas	Published parallax	77.250
LIT_PARALLAX_ERROR	f10.3	mas	Published parallax error	1.480
LIT_PARALLAXREFNAME	a19	...	Published parallax BibCode	2014PASP..126...15W
TMASSJ	f10.3	mag	2MASS <i>J</i> -band magnitude	12.934
TMASSJERR	f10.3	mag	2MASS <i>J</i> -band magnitude error	0.024
TMASSH	f10.3	mag	2MASS <i>H</i> -band magnitude	12.127
TMASSHERR	f10.3	mag	2MASS <i>H</i> -band magnitude error	0.031
TMASSK	f10.3	mag	2MASS <i>K</i> -band magnitude	11.602
TMASSKERR	f10.3	mag	2MASS <i>K</i> -band magnitude error	0.025
WISEW1	f10.3	mag	ALLWISE <i>W1</i> -band magntiude	11.246
WISEW1ERR	f10.3	mag	ALLWISE <i>W1</i> -band magntiude error	0.023
WISEW2	f10.3	mag	ALLWISE <i>W2</i> -band magntiude	10.971
WISEW2ERR	f10.3	mag	ALLWISE <i>W2</i> -band magntiude error	0.021
WISEW3	f10.3	mag	ALLWISE <i>W3</i> -band magntiude	10.505
WISEW3ERR	f10.3	mag	ALLWISE <i>W3</i> -band magntiude error	0.056
GUNNG	f10.3	mag	PANSTARRS <i>G</i> -band magntiude	21.955
GUNNGERR	f10.3	mag	PANSTARRS <i>G</i> -band magntiude error	0.061
GUNNR	f10.3	mag	PANSTARRS <i>R</i> -band magntiude	19.748
GUNNRERR	f10.3	mag	PANSTARRS <i>R</i> -band magntiude error	0.013
GUNNI	f10.3	mag	PANSTARRS <i>I</i> -band magntiude	17.375
GUNNIERR	f10.3	mag	PANSTARRS <i>I</i> -band magntiude error	0.003
GUNNZ	f10.3	mag	PANSTARRS <i>Z</i> -band magntiude	15.925
GUNNZERR	f10.3	mag	PANSTARRS <i>Z</i> -band magntiude error	0.005
GUNNY	f10.3	mag	PANSTARRS <i>Y</i> -band magntiude	14.936
GUNNYERR	f10.3	mag	PANSTARRS <i>Y</i> -band magntiude error	0.006
PHOT_G_MEAN_MAG	f10.3	mag	<i>Gaia</i> DR2 <i>G</i> -band magntiude	17.807
PHOT_G_MEAN_MAG_ERROR	f10.3	mag	<i>Gaia</i> DR1 <i>G</i> -band magntiude error	0.002
PHOT_G_MEAN_FLUX	f10.1	–	<i>Gaia</i> DR2 <i>G</i> -band flux	1420.5
PHOT_G_MEAN_FLUX_ERROR	f8.1	–	<i>Gaia</i> DR1 <i>G</i> -band flux error	2.2
PHOT_BP_MEAN_MAG	f10.3	mag	<i>Gaia</i> DR2 BP-band magntiude	20.931
PHOT_BP_MEAN_MAG_ERROR	f10.3	mag	<i>Gaia</i> DR1 BP-band magntiude error	0.137
PHOT_BP_MEAN_FLUX	f10.1	–	<i>Gaia</i> DR2 BP-band flux	58.6
PHOT_BP_MEAN_FLUX_ERROR	f8.1	–	<i>Gaia</i> DR1 BP-band flux error	7.4
PHOT_RP_MEAN_MAG	f10.3	mag	<i>Gaia</i> DR2 RP-band magntiude	16.193
PHOT_RP_MEAN_MAG_ERROR	f10.3	mag	<i>Gaia</i> DR1 RP-band magntiude error	0.006
PHOT_RP_MEAN_FLUX	f10.1	–	<i>Gaia</i> DR2 RP-band flux	2676.0
PHOT_RP_MEAN_FLUX_ERROR	f8.1	–	<i>Gaia</i> DR1 RP-band flux error	15.1
GAIAGEST	f10.3	mag	Estimated DR2 <i>G</i> from SpT	17.978
PARALLAX	f8.2	mas	<i>Gaia</i> DR2 parallax	68.33
PARALLAX_ERROR	f5.2	mas	<i>Gaia</i> DR2 parallax error	0.13
PMRA	f8.2	mas yr ^{−1}	<i>Gaia</i> DR2 Proper motion in RA	24.49
PMRA_ERROR	f5.2	mas yr ^{−1}	<i>Gaia</i> DR2 RA proper motion error	0.25
PMDEC	f8.2	mas yr ^{−1}	<i>Gaia</i> DR2 Proper motion in Dec.	−136.91
PMDEC_ERROR	f5.2	mas yr ^{−1}	<i>Gaia</i> DR2 Dec. proper motion error	0.27

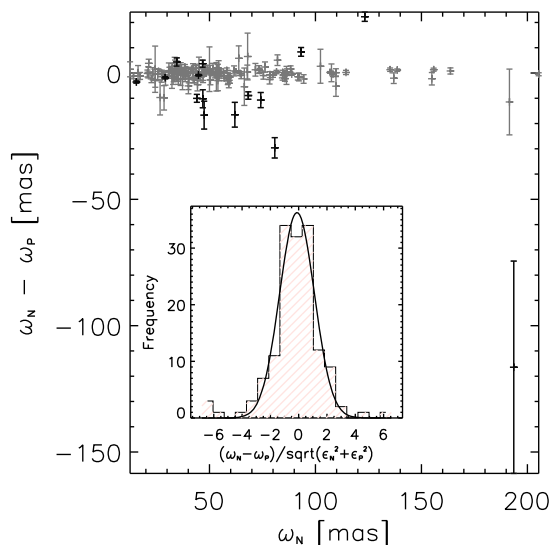


Figure 2. Differences between *Gaia* DR2 and published parallaxes versus *Gaia* DR2 parallaxes. Error bars are combined *Gaia* DR2 and published uncertainties plotted in grey. The large outlier is J1506+7027 discussed in the text. In black, all object with parallaxes differing by more than 2.5 times the combined uncertainties (listed in Table 4). The insert is a plot of the distribution of the ratio of parallax differences to combined uncertainties as shown in equation (1).

Here we report two new candidate members of this system, namely 2MASS J21192028–8145446 and 2MASS J211215980–8128452. Of them, 2MASS J21121598–8128452 was classified as M5.5 (Gagné et al. 2015), and would be the widest component of the system, with a projected separation of $\sim 62\,700$ au. No spectral classification is given for 2MASS J21192028–8145446, but since it is 0.61 mag fainter than 2MASS J21121598–8128452 we expect it to be an m6–7 dwarf; we use lowercase letters instead of the usual uppercase to indicate the spectral type is not based in spectroscopy (Lépine & Gaidos 2011; Alonso-Floriano et al. 2015). Its projected separation from the M1 primary is $\sim 31\,000$ au.

We can compute a lower limit for the binding energy using the known spectral types to estimate masses. For the M1 primary we assume a mass of $0.53 M_{\odot}$, and for the M5.5 a mass of $0.1 M_{\odot}$, by interpolating the updated version of table 5 from Pecaut & Mamajek (2013).² For the m6–7 dwarf, at the age of the system, the Baraffe et al. (2003) isochrones predict a mass in the $35\text{--}75 M_{\text{Jup}}$ range. We assume the upper limit of this mass range in the following analysis. For the L3 dwarf we adopt a mass of $15 M_{\text{Jup}}$, i.e. the upper limit of the range estimated by Deacon et al. (2016). We also conservatively assume the semimajor axis (a) to be equal to the observed projected separation (while in reality $s \leq a$). Under the above assumptions, the total binding energy for the system would be $U_g^* \gtrsim -1.5 \times 10^{33} J$, so the system would only be loosely bound (see e.g. Caballero 2009, fig. 1) and unlikely to survive Galactic tides. We can determine an expected lifetime for such a system using equation (18) from Dhital et al. (2010). We find that for the M5.5 the expected lifetime is ~ 2.9 Gyr, and for the m6–7 is ~ 5.8 Gyr.

An alternative explanation would be that these are simply members of the same young moving group. All four of these objects

Table 4. Objects with published parallax estimates differing by more than 2.5σ with the *Gaia* DR2 parallax.

Short Name	<i>Gaia</i> ϖ (mas)	Published ϖ (mas)
J0439–2353	80.79 ± 0.51	110.40 ± 4.00^a
J0445–3048	61.97 ± 0.18	78.50 ± 4.90^a
J0615–0100	44.80 ± 0.33	45.70 ± 0.11^b
J0805+4812	46.78 ± 0.96	43.10 ± 1.00^c
J1017+1308	34.56 ± 0.82	30.20 ± 1.40^c
J1155–3727	84.57 ± 0.19	104.38 ± 4.69^a
J1207–3932A	15.52 ± 0.16	19.10 ± 0.40^d
J1254–0122	74.18 ± 2.31	84.90 ± 1.90^e
J1359–4034	47.51 ± 0.27	64.18 ± 5.48^a
J1454–6604	93.22 ± 0.30	84.88 ± 1.71^f
J1506+7027	193.55 ± 0.94	310.00 ± 42.00^g
J1610–0040	29.14 ± 0.37	31.02 ± 0.26^h
J1717+6526	46.86 ± 0.62	57.05 ± 3.51^i
J1731+2721	83.74 ± 0.12	113.80 ± 7.00^j
J1807+5015	68.33 ± 0.13	77.25 ± 1.48^i
J2148+4003	123.28 ± 0.46	101.01 ± 1.78^k

Discovery references:

^aFaherty et al. (2012),

^bSahlmann et al. (2014),

^cDupuy & Liu (2012),

^dDucourant et al. (2008),

^eDahn et al. (2002),

^fDieterich et al. (2014),

^gMarsh et al. (2013),

^hDahn et al. (2008),

ⁱWang et al. (2014),

^jDittmann et al. (2014),

^kLiu, Dupuy & Allers (2016).

have indeed been selected as candidate members of the Tucana–Horologium Association by Gagné et al. (2015), while Deacon et al. (2016) argue that 2MASS J21265040–8140293 and TYC 9486–927–1 are members of the β Pictoris moving group. However, using *Gaia* updated astrometry and the BANYAN Σ online tool (Gagné et al. 2018), we find 0 per cent Tucana–Horologium and β Pictoris membership probability. The main reason for this discrepancy is probably that the four objects are approximately 5 pc further away than estimated using photometry in Gagné et al. (2015) and Deacon et al. (2016). Their *Gaia* proper motions on the other hand are consistent with the values used in those papers. Moreover, the initial membership assessments were conducted using BANYAN II (Gagné et al. 2014), and BANYAN Σ is known to provide more accurate membership probabilities (Gagné et al. 2018).

We find a non-zero probability membership only for the AB Doradus moving group, with probability in the range 4.5–10.5 per cent, but the reported age range for the system (10–45 Myr) is inconsistent with the age of AB Doradus (100–125 Myr; Luhman, Stauffer & Mamajek 2005). We expect tools such as BANYAN Σ to undergo a major overhaul following *Gaia* DR2 with the astrometry provided by *Gaia* strongly constraining the group kinematics. Further discussion of the true nature of this association is therefore deferred to a future paper.

(iii) Four systems consist of members of young moving groups and associations. 2MASS J01415823–4633574 forms a wide common-proper-motion pair with the M5.5 2MASS J01443191–4604318. Both objects are members of the Tucana–Horologium Association (with 99.5 per cent and 99.8 per cent membership probability, respectively; Gagné et al. 2015).

²http://www.pas.rochester.edu/emamajek/EEM_dwarf_UBVIJHK_color_s_Teff.txt.

Table 5. New candidate binary systems containing LT dwarfs, identified in *Gaia* DR2.

Discovery Name	ρ (arcsec)	RA, Dec. ($^{\circ}$)	Spec. Type	G (mag)	ϖ (mas)	μ_{tot} (mas yr $^{-1}$)	θ_{μ} ($^{\circ}$)
2MASS J01415823–4633574	2377.2	25.4933685, –46.5661305	L2.0	20.02	27.4 \pm 0.5	124.7	111.9
4954453580066220800		26.1336010, –46.0756886	–	15.67	25.9 \pm 0.1	117.3	111.3
2MASS J02235464–5815067		35.9785858, –58.2519130	L1.5	20.22	24.4 \pm 0.6	105.6	99.5
UCAC4 159-002053	1532.6	35.2149151, –58.3948241	M3	12.57	22.7 \pm 0.0	97.2	99.7
2MASS J02251947–5837295	1499.0	36.3319895, –58.6249554	M9	18.41	24.3 \pm 0.2	102.0	99.1
2MASSI J0518461–275645	1007.2	79.6925197, –27.9460523	L1.0	20.48	17.3 \pm 0.8	32.6	98.7
2954995674982867968		79.8573963, –28.1850235	–	15.11	17.6 \pm 0.1	32.6	98.9
2MASS J08430796+3141297	819.5	130.7828536, 31.6913490	L2.5	20.91	14.8 \pm 2.3	67.9	230.3
709905940243414400		130.6127152, 31.8671235	–	17.47	10.2 \pm 0.2	73.1	235.1
2MASS J09073765+4509359	301.1	136.9073579, 45.1597676	M9.0	18.99	26.3 \pm 0.4	76.8	118.1
TYC 3424-215-1		137.0239116, 45.1753675	–	9.22	27.0 \pm 0.1	80.2	123.5
2MASS J09175035+2944455	1684.7	139.4595607, 29.7456267	L0.0	20.74	18.5 \pm 2.4	81.2	215.9
698766581783119872		139.8773149, 29.4505981	–	17.65	12.8 \pm 0.3	74.4	227.6
2MASS J11414410+4116568	163.5	175.4341457, 41.2822985	L0.0	20.36	13.2 \pm 1.1	60.1	133.9
HD101620		175.4433423, 41.2374147	F5	6.79	12.7 \pm 0.0	58.7	130.9
SDSS J124514.95+120442.0	96.4	191.3122876, 12.0781604	L1.0	20.98	12.3 \pm 3.0	54.8	191.1
SDSS J124520.60+120531.3		191.3358362, 12.0918479	DA	18.29	12.2 \pm 0.3	54.8	186.9
ULAS J124531.54+015630.9	8.2	191.3813059, 1.9418705	–	20.61	13.5 \pm 1.2	76.0	234.7
3702489721592680832		191.3791501, 1.9411384	–	12.86	13.2 \pm 0.0	75.6	235.1
WDS J15200–4423A	1.0	230.0053261, –44.3801380	18.29	L1.5	54.5 \pm 0.2	736.7	238.6
WDS J15200–4423B		230.0054769, –44.3798731	19.82	L4.5	53.7 \pm 0.6	753.4	238.6
2MASS J16325610+3505076	57.1	248.2342852, 35.0851446	L1.0	19.47	28.6 \pm 0.3	107.8	124.2
HD149361		248.2192979, 35.0750997	K0V	8.03	29.0 \pm 0.0	107.4	125.6
2MASS J21265040–8140293		321.7115878, –81.6752636	L3.0	20.72	29.2 \pm 0.9	128.5	153.9
TYC 9486-927-1	217.5	321.3662989, –81.6414894	M1.0V	10.81	29.3 \pm 0.1	123.2	150.9
2MASS J21192028–8145446	1022.2	319.8360962, –81.7628668	–	14.65	29.0 \pm 0.1	126.0	153.3
2MASS J21121598–8128452	2045.7	318.0681165, –81.4797055	M5.5	14.04	28.6 \pm 0.1	123.8	155.0
DENIS-PJ220002.05–303832.9A	1.0	330.0096692, –30.6428312	M9.0	18.44	25.4 \pm 0.4	247.2	104.9
DENIS-PJ220002.05–303832.9B		330.0096946, –30.6425580	L0.0	19.04	25.3 \pm 0.5	253.7	105.6
ULAS J230818.73+062951.4	3.8	347.0781929, 6.4973599	–	18.06	24.7 \pm 0.3	118.5	162.3
2665079816223169664		347.0788922, 6.4981654	–	13.47	24.1 \pm 0.1	119.8	160.5
2MASS J23225299–6151275	16.6	350.7215915, –61.8579914	L2.5	20.68	23.2 \pm 1.0	114.6	135.7
2MASS J23225240–6151114		350.7191431, –61.8535236	M5	14.90	23.6 \pm 0.1	110.3	135.2

2MASS J02235464–5815067, 2MASS J02251947–5837295, and UCAC4 159-002053 are also members of the Tucana–Horologium Association (with membership probability of 99.9 per cent, 99.7 per cent, and 99.9 per cent respectively). 2MASSI J0518461–275645 and 2954995674982867968 are both members of Columba (99.9 per cent membership probability for both). These are very wide systems, with typical projected physical separations, $s > 50\,000$ au, and so the nature of these systems is uncertain. Finally, 2MASS J23225299–6151275 and 2MASS J23225240–6151114 are also members of the Tucana–Horologium Association (with membership probability of 96.7 per cent and 99.9 per cent, respectively), but form a much tighter pair with projected physical separation of ~ 710 au. This system is therefore unequivocally bound.

These systems will provide valuable benchmark systems to constrain atmospheric models and retrieval techniques. However, we have not tried to produce a complete catalogue of binary systems containing UCD objects. As discussed in Section 2 our criteria fails for the binary systems GJ 1048 A/B and G 239–25 A/B in both cases because the modulus of the difference in proper motions is greater than 10 per cent. Hence the production of a complete catalogue will require more sophisticated procedures, such as taking into account the orbital motions of the components based on their predicted masses and distances.

4 PHOTOMETRIC EXAMINATION

4.1 Absolute G versus $G - G_{RP}$

The most complete set of magnitudes for our UCD objects is in the *Gaia* passbands, and these are also a new set of bands for studying these objects. In Fig. 3 we plot the *Gaia* DR2 absolute magnitude M_G versus colour $G - G_{RP}$.

The $G - G_{RP}$ colour shows a tight correlation that gradually increases from 1.5 to 2.1 mag as one descends the main sequence. The standard deviation in colour per absolute magnitude bin varies from 0.06 to 0.13 mag. In the *Gaia* DR2 there are no published magnitude uncertainties to underline to the user that the magnitude uncertainties are not symmetric. We have transformed the flux uncertainties into magnitude upper and lower bounds and found a median error of 0.02 mag, indicating that the majority of the observed standard deviation is due to intrinsic variations, which is in line with the intrinsic spread seen in similar relations (Filippazzo et al. 2015; Faherty et al. 2016).

There are a number of outliers in Fig. 3. In particular, there are six UCD outliers that are 3σ from the ‘main-sequence’ #x00A0; locus. We label them in the figure, and discuss them below:

(i) J0543+6422 (2MASS J05431887+6422528) was spectroscopically found to be non-binary in Bardalez Gagliuffi et al. (2014). However, in the *Gaia* DR2 there is an object detected (287767756635519488) at a separation of 0.6 arcsec, slightly

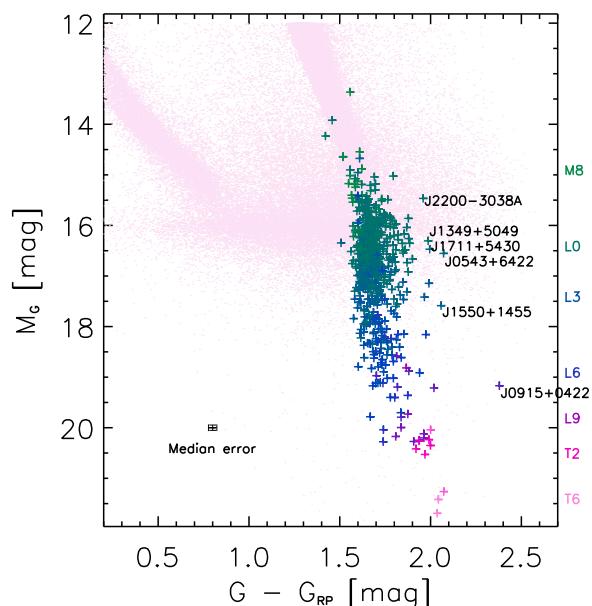


Figure 3. Colour–magnitude diagrams for absolute G versus $G - G_{\text{RP}}$. The light green points are all objects nominally within 100 pc brighter than $M_G = 12$ mag from *Gaia* DR2 regardless of quality flags, to delineate the white dwarf and main sequences. The crosses are the GUCDS entries colour coded by spectral type as indicated on the right hand side at the respective absolute magnitudes. Plotted in the lower left are median error bars.

Table 6. J1711+5430 and NLTT 44368 *Gaia* DR2 parameters.

Name	ϖ (mas)	$\mu_{\alpha} \cos \delta$ (mas yr $^{-1}$)	μ_{δ} (mas yr $^{-1}$)
J1711+5430	22.06 ± 0.60	-48.71 ± 1.70	206.73 ± 1.904
NLTT 44368	21.14 ± 0.04	-61.62 ± 0.12	211.31 ± 0.092

brighter ($G = 18.96$ versus 18.97 mag) and slightly redder ($G - G_{\text{RP}} = 2.11$ versus 2.07 mag) but with no parallax estimate. The uncertainty in position is very high (20.8 versus 1.1 mas in declination), consistent with a nearby object that is being constrained to having a zero parallax. The number of observations is however very different, 42 versus 191, indicating that it may be the same object with observations assigned to two `Source_IDs`. The red colour and similar magnitude are consistent with both being an equal-mass binary with a separation of 0.6 arcsec or a single source with two `Source_IDs`. There is no most probable scenario for this object and it is a prime candidate for observation with a ground-based adaptive optics system to confirm if it is actually a binary system.

(ii) J0915+0422 (2MASS 09153413+0422045) is a binary system of two L6 dwarfs with a separation of 0.73 arcsec (Reid et al. 2006), at a distance of 18 pc. In the *Gaia* DR2 data there is the probable match (`Source_ID` 579379032257250176) 0.3 arcsec from the GUCDScat position, 579379032258066432 at a separation of 0.6 arcsec, and 579379027962863104 at a separation of 3.3 arcsec. Neither of the more distant matches have full solutions and the object at 3.3 arcsec is not red ($G - G_{\text{RP}} = 1.4$ mag), while the closer detection has only a G magnitude. The number of along-scan observations are 111, 80, and 80 for the probable, close, and more distant match, respectively – this difference in the

number of observations for objects close on the sky is large but may not be indicating anything other than the downloading of *Gaia* observations are complicated. All objects may be real and, in some scan angles, *Gaia* may resolve them and in others may not. The position uncertainties are very different. For example in declination they are 0.9 , 25.6 , and 1.3 mas, respectively. The high uncertainty is consistent with a nearby object that is being constrained to having a zero parallax.

The most probable scenario is that 579379027962863104 (at 3.3 arcsec) is a background star or galaxy and 579379032258066432 (at 0.6 arcsec) is the binary companion from Reid et al. (2006), but it could also turn out that the changing scanning direction correlates with the separation, and the matching of the observations were compromised – hence the lower number of along-scan observations. The source of the larger $G - G_{\text{RP}}$ colour for this system compared to a normal L6 is because the G_{RP} and G_{BP} magnitudes are found from integration of the G_{RP} and G_{BP} fluxes in 3.5×2.1 arcsec windows, and there is no provision for multiple sources in the same window (Evans et al. 2018). Therefore, an excess in G_{RP} for close binary systems is expected. Indeed, in the $G_{\text{RP}} - J$ or $G_{\text{RP}} - z$ colours J0915+0422 does not stand out, which is expected if the system is made of similar objects and not resolved in both passbands that make up the colour. If we assume the system is an equal-mass binary the G_{RP} of an individual component will be 0.75 mag fainter, which is consistent with the 0.6 mag offset from the main sequence in Fig. 3. We therefore conclude that the *Gaia* G_{RP} for this object is the total system magnitude rather than the individual component magnitude.

(iii) J1349+5049 (2MASS J13492525+5049544) has no literature indication of binarity and there are no other *Gaia* DR2 detections nearby. The only *Gaia* DR2 indication that may suggest a non-single solution is that it has the highest goodness-of-fit statistic for the along-scan observations of 84 (a ‘good’ value would be 3), and the highest astrometric excess noise value for this sample.

(iv) J1550+1455 (2MASS J15500845+1455180) is a known L3.5 + L4 system with a separation of 0.9 arcsec (Burgasser, Dhital & West 2009). In the *Gaia* DR2 there is a detection of an object (1192782134013894144) at that separation from J1550+1455, but it has no parallax, G_{RP} , or G_{BP} magnitudes. The position uncertainties are not very high and both the probable match and the companion have over 200 observations, so the two of them are probably real. The very red colour of J1550+1455 could be due to the G_{RP} magnitude including flux from both components.

(v) J1711+5430 (NLTT 44368B) was predicted to be a companion to NLTT 44368, an M3 at 90.2 arcsec based on proper motions (Deacon et al. 2014). In Table 6 we report the *Gaia* DR2 parallaxes and proper motions. While the values are close, the differences in proper motions are significant and these two objects do not pass our binarity test developed in Section 3. The difference in proper motion may be due to binarity in J1711+5430. However, apart from its red $G - G_{\text{RP}}$ colour for its M_G magnitude, there is no published indication of unresolved binarity, there are no other *Gaia* DR2 detections nearby, and the only *Gaia* DR2 parameter that may be indicating multiplicity is the duplicate flag, which is set to 1.

(vi) J2200–3038A, as noted in Section 3, is the brightest component of the M9 + L0 system DENIS-P J220002.05–303832.9AB with a separation of 1.1 arcsec (Burgasser & McElwain 2006). The second component does not have G_{RP} or G_{BP} magnitudes, and the G_{RP} flux of the primary component probably is the combination of both elements.

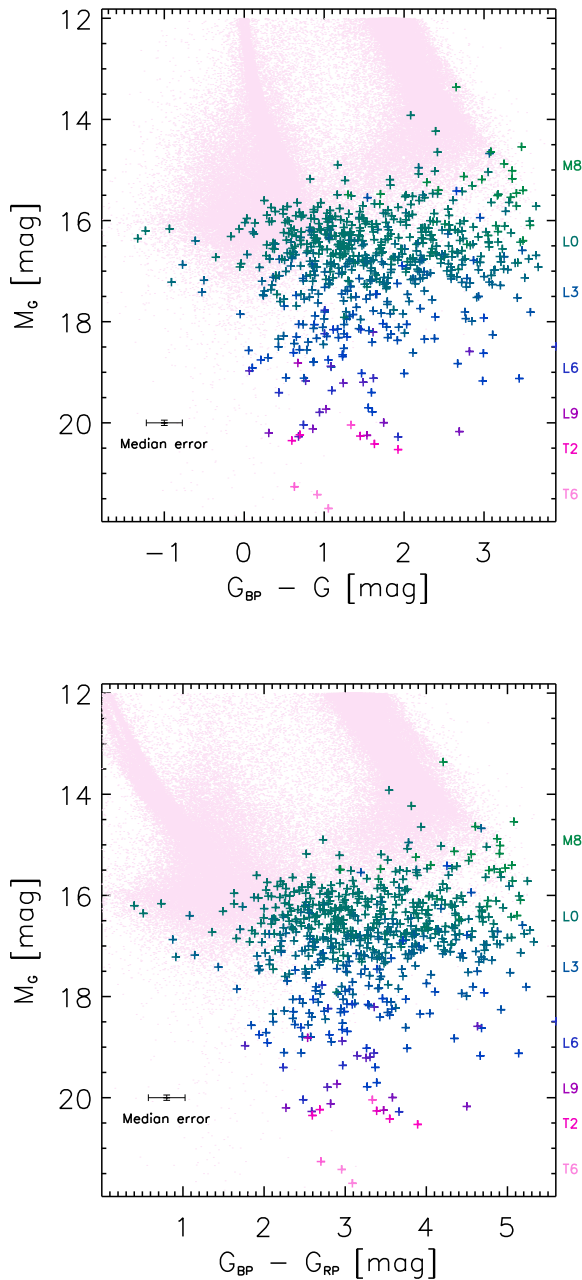


Figure 4. Colour–magnitude diagrams for absolute G versus $G_{BP} - G$ (top) and $G_{BP} - G_{RP}$ (bottom). The light pink points are all objects within 100 pc, the crosses are the GUCDScat entries colour coded by spectral type as indicated on the right hand side. Plotted in the lower left are error bars that are equivalent to the median uncertainty.

4.2 Absolute G versus $G_{BP} - G$

In Fig. 4 we plot M_G versus $G_{BP} - G_{RP}$ and $G_{BP} - G$ colours, which have a strikingly higher dispersion relative to Fig. 3 for a similar baseline in colour. The standard deviation in colour varies from 0.6 to 1.0 mag, while the median formal error is only 0.2 mag. We cannot assign this larger standard deviation to intrinsic variations as there is no indications of this phenomenon in the literature for similar colour baselines. In Gaia Collaboration (2018b) they noted the larger scatter but merely commented that these objects have very low flux in the G_{BP} wavelength range, making them intrinsically imprecise, which is evident in the comparison of the three colour–

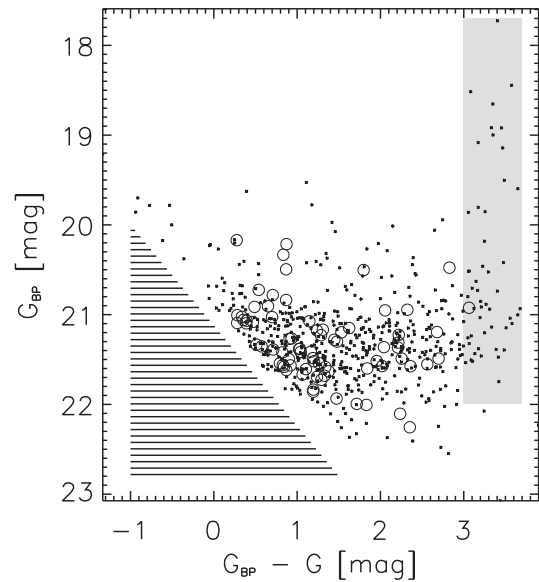


Figure 5. Top: G_{BP} versus $G_{BP} - G$ for all objects. The hashed area is where objects are missed due to the G -band magnitude limit. Open circles are objects with SDSS counterparts. The grey shaded area shows where we expect the $G_{BP} - G$ colour of these objects to occupy.

magnitude plots. However, the scatter in Fig. 4 is present even for relatively bright UCDs, $G_{BP} \sim 19.5$, and the uncertainties are not consistent with such a large scatter.

Our sample is faint and, particularly in the blue band, at the limit of what the *Gaia* team considers reliable photometry. If we apply the relative flux error selection that Gaia Collaboration (2018b) applied, e.g. `phot_g_mean_flux_over_error` > 50, `phot_rp_mean_flux_over_error` > 20, and `phot_bp_mean_flux_over_error` > 20, then of the 695, 660, and 660 objects with published magnitudes in the G , G_{BP} , and G_{RP} bands only 693, 14, and 602 would remain. In addition they only constrained the flux ratio $(I_{G_{BP}} + I_{G_{RP}})/I_G$ (`phot_bp_rp_excess_factor`) to the range $1.0 + 0.015(G_{BP} - G_{RP})^2 < \text{phot_bp_rp_excess_factor} < 1.3 + 0.06(G_{BP} - G_{RP})^2$, which would reduce our 660 sample to only 218. Indeed for the fig. 9 of Gaia Collaboration (2018b) they did not apply this filter on fluxes as the size of the sample would have been significantly reduced.

In Arenou et al. (2018) they estimated a unit-weight uncertainty³ of 1.3 assuming that the widths of main sequences in Galactic clusters were due solely to photometric uncertainties. The large standard deviation of the $G_{BP} - G$ colour with respect to the median uncertainty implies a unit-weight uncertainty of ~ 3 . Therefore, either there is a large intrinsic scatter or the uncertainties of the G_{BP} are significantly underestimated.

In Fig. 5 we show the $G_{BP} - G$ colour versus the G_{BP} magnitude for all UCDs. We expect the colour to be clustered at a $G_{BP} - G \sim 3$ mag, as outlined by the grey box. The brightest examples fall within this range, but for $G_{BP} > 19.5$ mag the UCDs appear to be spread evenly. To investigate the possibility that the observed scatter is intrinsic we examine the SDSS magnitudes. In Fig. 6 we show that the G_{BP} band coverage is roughly equal to the combined SDSS g and r coverage. We have taken those objects from our

³The ‘unit-weight uncertainty’ is the ratio of the calculated unit weight and an independent estimate of the true error.

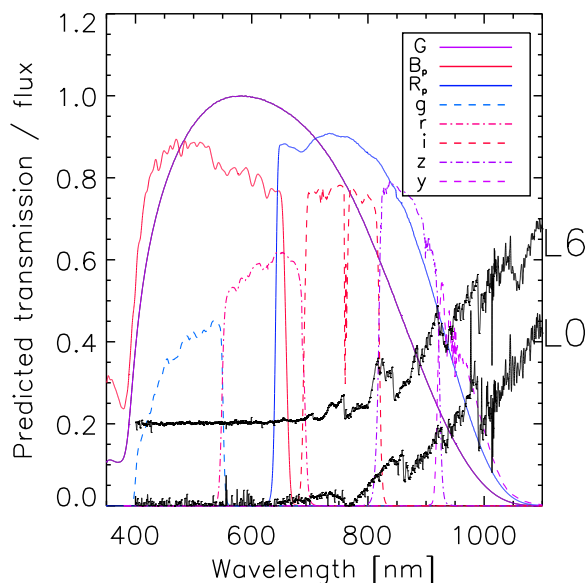


Figure 6. Normalized filter and optical transmission for the *Gaia* and Gunn (used in the SDSS and PS1 surveys) passbands. Colours and passbands as indicated in the legend and normalization of the two sets of filters are different and chosen to separate the two blocks. The spectra are from X-Shooter for the L0 dwarf J2344–0733 (*bottom*) and the L6 dwarf J0006–6436 (*top*).

sample that have g and r magnitudes in the SDSS, and constructed a pseudo- G_{BP} magnitude, dubbed $SDSSG_{BP}$, by adding the fluxes in the g and r SDSS bands. We restricted the selection to objects with uncertainties in G_{BP} , r , and g to less than 0.6 mag, which provided a sample of 75 M9–L1 objects with G_{BP} between 20.17 mag and 22.25 mag. The objects with SDSS counterparts are plotted as open circles in Fig. 5.

In the top panel of Fig. 7, the objects with $SDSSG_{BP} - G$ colours (filled circles) centre on ~ 2 mag with a dispersion of 0.2 mag that increases slightly as the objects get fainter. The $G_{BP} - G$ colours of the same objects (open circles) show a lack of clustering with a dispersion of 0.70 mag, even though the median error is 0.25 mag. The offset between the $SDSSG_{BP} - G$ colour at ~ 2 mag and the predicted $G_{BP} - G$ colour at ~ 3 mag is not unexpected, as the g and r passbands cover the same spectral range as G_{BP} , but the combined profile is different. Besides, the SDSS magnitudes are on the AB magnitude system, while the zero-point of the *Gaia* magnitudes are set by Vega.

Another indication of problems in the G_{BP} passband for faint red objects can be seen in fig. 33 of Arenou et al. (2018), where the main sequence of the Alessi 10 cluster deviates from the expected path at $G_{BP} \sim 19.5$ mag. As this cluster is considered a dense field they cited a number of possible contributing factors (underestimated sky background, overlapping spectra, extended objects, and blended objects), but these factors would not be appropriate for our targets, which are primarily in low-density regions.

In order to test the reliability of G_{BP} in another cluster, we constructed a sample of the Praesepe cluster members using only the astrometric parameters in the *Gaia* DR2. We selected all objects with (α, δ) in the range $(126\text{--}135, 16\text{--}24)^\circ$, ϖ in the range 3–7 mas and $(\mu_\alpha \cos \delta, \mu_\delta)$ in the ranges $(-30$ to 40, -10 to 18) mas yr^{-1} based on the membership sample provided in Gaia Collaboration (2018b), resulting in 1336 members listed here. There was no limit made on the quality of the photometry, as this would have removed

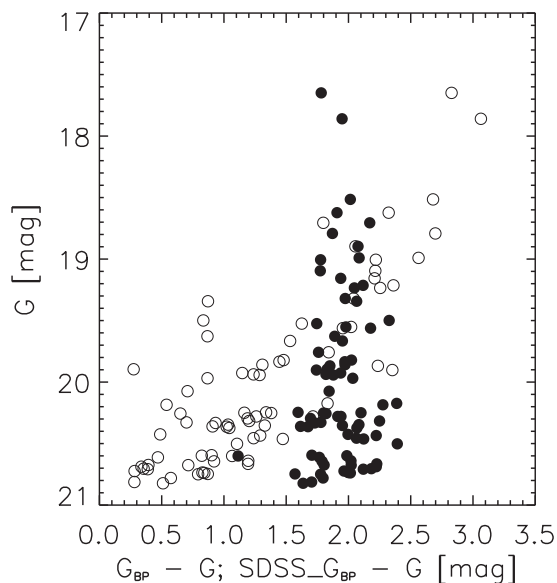
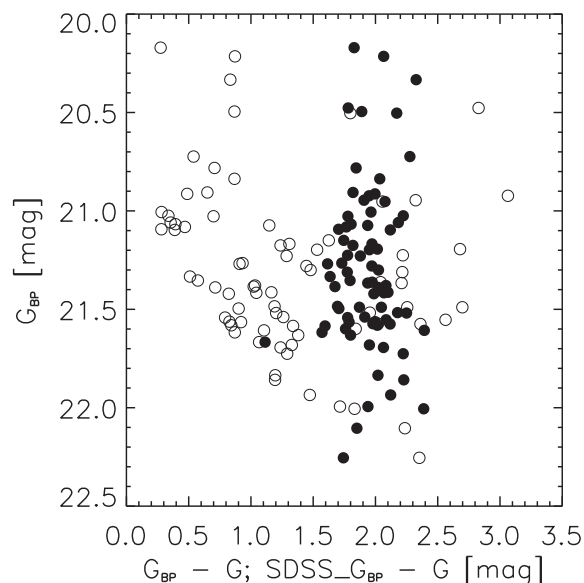


Figure 7. *Top*: zoom on the objects with SDSS magnitudes from Fig. 5. Open circles as before using G_{BP} versus $G_{BP} - G$; filled circles are the same objects however plotting G_{BP} versus $SDSSG_{BP} - G$. *Bottom*: same as top panel figure but plotting G instead of G_{BP} on the ordinate.

all of the faint members. This cluster was chosen as it has a proper motion that is significantly different from the field so we can be quite confident that the sample is dominated by Praesepe members. In Fig. 8 we plot M_C versus $G_{BP} - G$ in the top panel, where a deviation of the main sequence from the expected path for faint red objects is seen, as in Arenou et al. (2018) for Alessi 10. The authors colour coded the Alessi 10 members by the number of observations in the G_{BP} band, and noted that the objects with the lowest number of observations are predominantly in the deviated region. We have made the same colour coding in Fig. 8, but the objects with lower numbers of observations are not confined to the deviated part. More examples are required to see if the correlation of deviation with number of observations observed in Alessi 10 is significant.

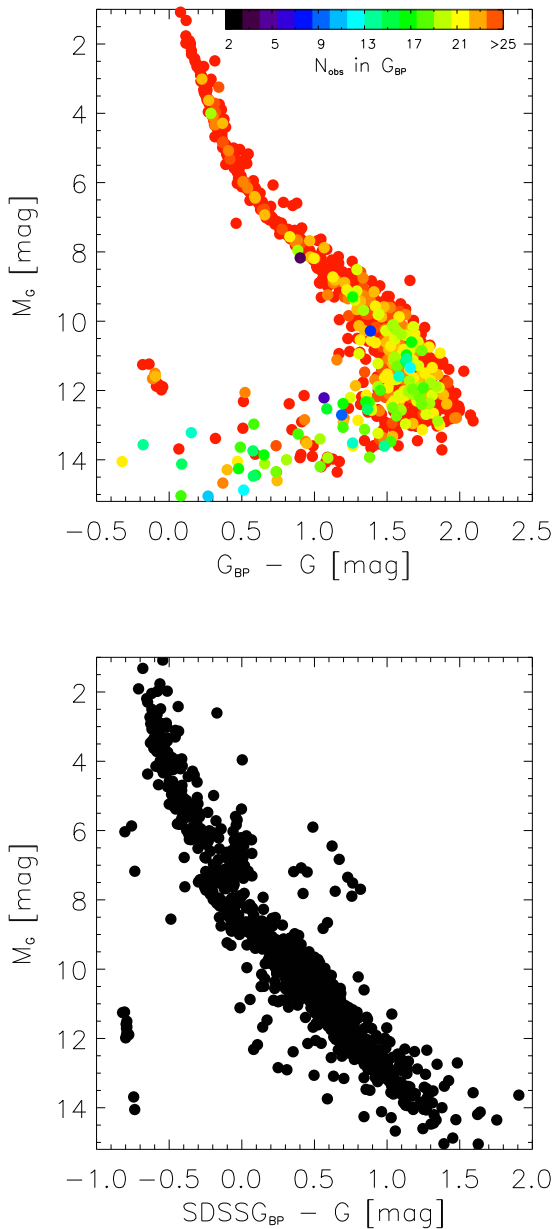


Figure 8. *Top:* M_G versus $G_{BP} - G$ for members of Praesepe cluster selected astrometrically. The colour coding follows the number of observations in the G_{BP} band as indicated in the colour bar. *Bottom:* M_G versus $SDSSG_{BP} - G$ for the same sample of objects as the top panel.

In the lower panel of Fig. 8 we plot the same objects using $SDSSG_{BP}$ instead of G_{BP} . The spread in the main sequence is larger than the top panel because the SDSS magnitudes are less precise; this is also a very dense region that adversely impacts the SDSS measurements compared to the *Gaia* DR2 ones. The distinct discontinuity in the main sequence at $M_G \sim 7.0$ mag is due to the brightest objects being saturated in the SDSS. However, the lower main sequence in $SDSSG_{BP}$ follows an expected increasingly redder path for fainter objects not unexpectedly deviated path of the top panel.

We examined other samples of selected red sources and found the $G - G_{BP}$ colour was significantly noisier than the $SDSSG_{BP} - G_{BP}$ for the late-type M dwarfs catalogue from Schmidt et al. (2010) but the colours are consistent for early M dwarfs (West et al. 2011), carbon stars (Downes et al. 2004), white dwarfs (Gentile Fusillo

et al. 2019), and quasars (Secrest et al. 2015). As a result, we find the G_{BP} and uncertainty values are inconsistent only for very red, faint, objects.

The G_{BP} flux, from which the magnitude is derived, is the mean of the integrated spectra in the aforementioned 3.5×2.1 arcsec windows over all the observations. These objects are extremely faint in G_{BP} , many are background limited, and one possible reason for underestimating the G_{BP} may be because the error of the mean is dominated by the variation of the background flux, not by the variation of the objects flux. Another possibility is the position of the geometric windows are placed for the G_{BP} and G_{RP} filters using the *Gaia* G position, and perhaps the very red colour leads to a systematic offset in the G_{BP} window position.

Since the G_{BP} value comes essentially from aperture photometry, any detection level is crucially dependent on the background determination. A typical example of the differing fluxes can be seen in Table 3 for J1807+5015. It has fluxes of 1420.5, 58.5, and 2676.0 $\text{erg cm}^{-2} \text{s}^{-1} \text{Hz}^{-1}$ for the I_G , $I_{G_{BP}}$, and $I_{G_{RP}}$, respectively. As our objects are significantly above background in both the G and G_{RP} passbands, the simplest explanation is that a G_{BP} magnitude is included when robust G and G_{RP} detections are made, even if the G_{BP} detection is not itself significant, hence the derived G_{BP} magnitudes are determined by the background more than by the object. There is considerable complexity in the derivation and calibration of *Gaia* magnitudes and we conclude that any use of the G_{BP} passband for faint red objects must be made with caution and do not use it further for this work.

4.3 Colour–magnitude diagrams using external magnitudes

In Figs 9–11 we plot the colour combinations of the G band and the PS1, 2MASS, and AllWISE magnitudes versus absolute G magnitudes for the GUCDScat objects. Within each sequence of M_G absolute magnitude comparisons with external photometry we have set the relative range on the axes to be the same to simplify inter-comparisons. In each graph we have indicated on the left hand axis the average spectral type corresponding to the M_G for the main bulk of stars. Old, young, or binary systems do not correspond to this scale. If we replace G with G_{RP} the overall trends do not change.

In the last panel of each sequence we indicate spectral typing qualifications in the literature with the use of different symbols. For each entry in a binary system we plot as brown squares those unresolved binaries or systems with angular separations $\rho \leq 1$ arcsec on the assumption that ground-based programs are unable to extract the magnitudes of the different components if the separation is smaller. This is not always the case: e.g. an GUCDScat system has a nominal separation of $\rho > 1$ arcsec but it is not resolved and the magnitude is a combined value: or, the GUCDScat system has a $\rho < 1$ arcsec but the published magnitudes are of the separate components. We assumed that entries that have the gravity indicators γ , β (Cruz, Kirkpatrick & Burgasser 2009), ‘int-g’ or ‘vl-g’ (Allers & Liu 2013), or that are confirmed members of known moving groups are young and we have plotted them as upright triangles with colours as indicated in the legend. Finally, we assumed objects listed as subdwarfs or with $V_{\text{tan}} > 90 \text{ km s}^{-1}$ are old, and have plotted them as diamonds.

4.3.1 *Gaia* and *Pan-STARRS* PS1 magnitudes

We limit our examination for the PS1 catalogue to the i , z , and y passbands, because we find that 50 per cent and 30 per cent of the

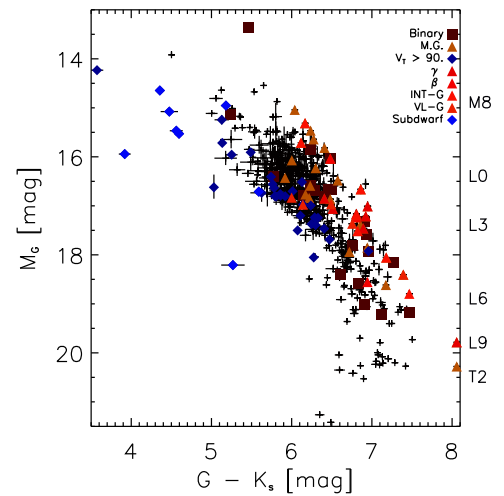
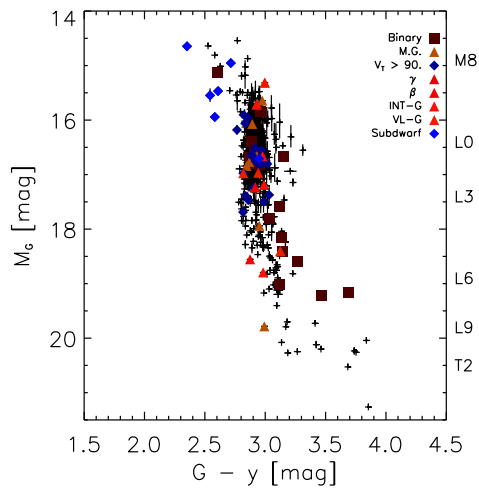
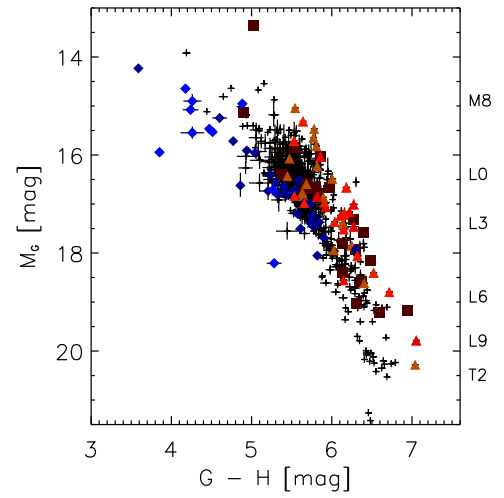
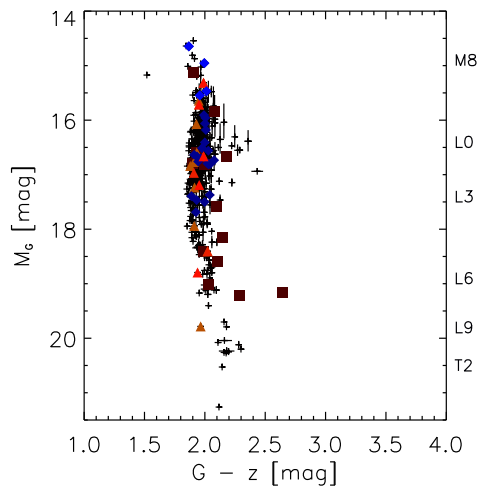
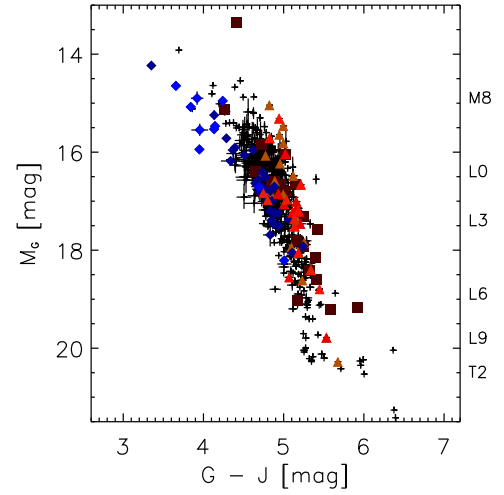
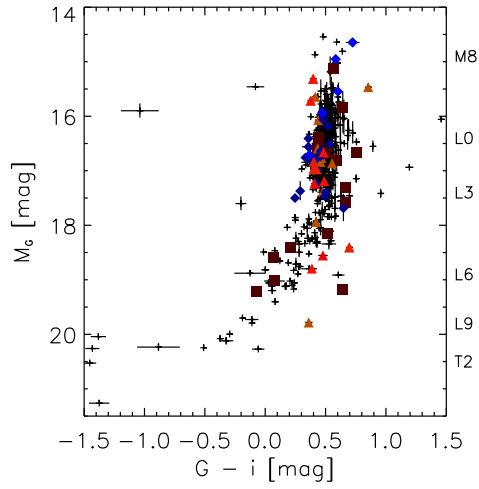


Figure 9. Colour–magnitude diagrams. G -band absolute magnitude as a function of $G - i$, $G - z$, and $G - y$ from the Pan-STARRS PS1. The legend in the third panel indicates the symbols used for spectral type qualifications, binarity, and high tangential velocity objects.

Figure 10. Same as Fig. 9 but for $G - J$, $G - H$, and $G - K_s$ colours from the 2MASS PSC.

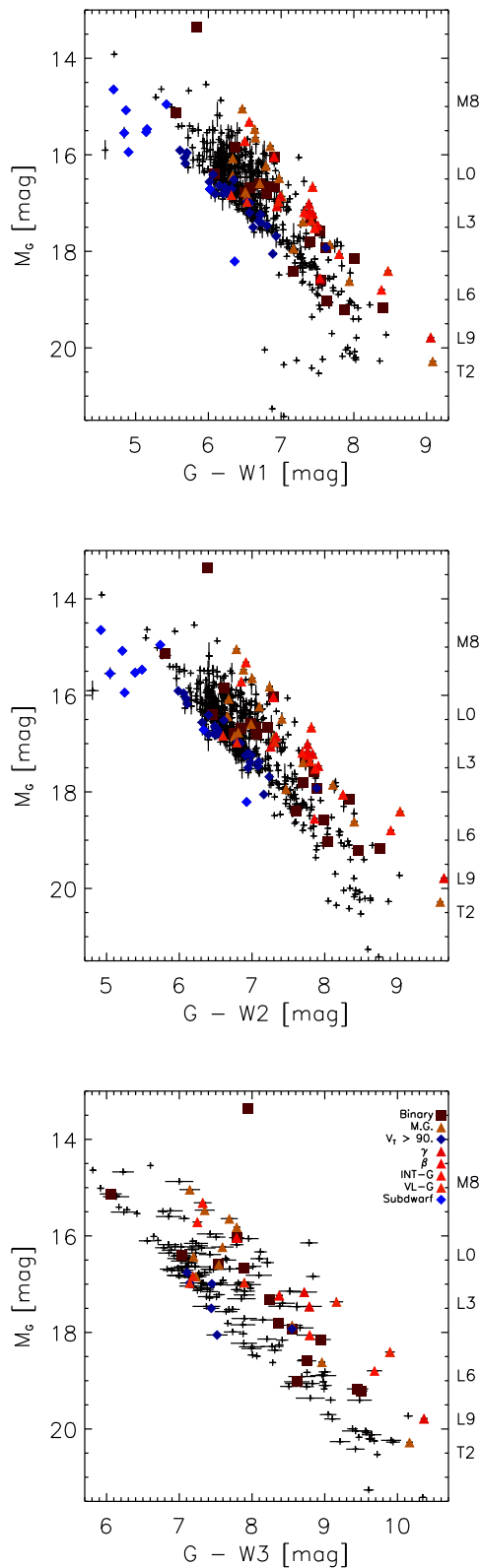


Figure 11. Same as Fig. 9 but for $G - W1$, $G - W2$, and $G - W3$ colours from the *WISE* AllWISE catalogue.

values in g and r , respectively, have bad quality flags or do not have error estimates. As shown in Fig. 6, the G band has significant sensitivity in these three PS1 bands and from that plot the effective wavelength of G appears to be bluer than r . However, the effective wavelength is object dependent and, on average, for L dwarfs the G band effective wavelength is very close to that of i .

In Fig. 9 the sequence for $15.5 < M_G < 18$ mag, roughly L0–L4, has remarkably constant $G - i$, $G - z$, and $G - y$ colours with widths of 0.07–0.08 mag. The earlier M dwarfs and later LT dwarfs deviate to bluer and redder colours, respectively. The objects with old and young spectral characteristics have dispersions of 0.08 mag in the $G - i$ and $G - y$ colours and up to 0.04 mag in $G - z$. Even though the overlap of all objects is quite significant, there is some correlation with the old and young dwarfs, being consistently on one side or the other of the main bulk of objects. For types later than L6 ($M_G > 18$ mag) in the bluer $G - i$ and redder $G - y$ colours, the deviations from the fixed colours of the earlier types reaches 0.5 mag and the trend increases with cooler spectral types. These colours can be useful for spectral type differentiation of late L and T dwarfs. Alternatively $G - z$ offers an almost constant value from $M_G = 15$ to 20 mag.

4.3.2 Gaia and 2MASS PSC magnitudes

Fig. 10 is the sequence of G absolute magnitude comparisons with G –2MASS colours. The mean colours vary by ~ 1.5 mag in all three relations. The dispersion increases from 0.16, 0.23, and 0.30 mag for the $G - J$, $G - H$, and $G - K_s$, respectively. The mean colour for the old and young samples separates by 0.6, 1.0, and 1.2 mag for the $G - J$, $G - H$, and $G - K_s$ colours, respectively. The underlying sequences maintain relatively linear relations with increasing slopes as the baseline colours increases. Overall, for L dwarfs all three colours continue to get redder as the objects get fainter in G . At the L–T boundary the three colours vary differently: redder in $G - J$, unchanging in $G - H$, and a turn around to bluer colours in $G - K_s$. The two ‘young’ objects (J0355+1133, Cruz et al. 2009 and J2148+4003, Kirkpatrick et al. 2010) along with the bulk of other objects with young indicators continue to move redward in all three colours. A primary cause of the increased spread in colours from $G - J$, through $G - H$, to $G - K_s$ plausibly corresponds to H - and K_s -band suppression from atomic and molecular absorption of methane and H_2 collision-induced absorption (e.g. Murray et al. 2011), which leads to relatively brighter H and K_s bands for the lower gravity young objects and in turn redder colours relative to the higher gravity older objects.

4.3.3 Gaia and AllWISE magnitudes

The G –AllWISE colour–magnitude diagrams are marked by a drop in objects with *WISE* magnitudes (648 in $W1$, 649 in $W2$, 446 in $W3$). The sharper lower bound in the main sequence of $G - W3$ indicates that the J , H , K , $W1$, $W2$ bands are more complete than *Gaia* for these objects, while the $W3$ band is incomplete. The blueward trend for late L and T dwarfs seen in $G - K_s$ is still evident in $G - W1$, but in $G - W2$ and $G - W3$ the trend turns again redward, indicating that temperature begins to dominate the spectral energy distribution as it does in stars with spectral types M or earlier.

The width of the main sequence in the M_G versus G –AllWISE colour–magnitude diagrams continues to increase as it does in the M_G –2MASS ones. The mean G –AllWISE colours vary by ~ 2.5 mag and their dispersions vary from 0.4 to 0.6 mag. The mean

colours of the old and young samples separate by 1.4 mag and have dispersions of 0.7 mag. The shallower depth of the $W3$ band makes it impossible to quantitatively characterize the $G - W3$ colour, but the visible trends are consistent with a continuation of an increasing dispersion and separation.

4.3.4 Colour–magnitude diagrams summary

The remarkably tight sequence in many field objects for $M_G = 17.5$ – 19 mag seen in the Fig. 9, M_G versus $G - z$, reappears in Fig. 10, M_G versus $G - H$ and $G - K_s$, manifesting as two distinct sequences for the youngest and oldest objects. There is a notable concentration of older objects that have largely cooled to follow a relatively narrow temperature versus luminosity sequence. The existence of these sequences and the range of objects between them, which presumably have a younger age or are binaries, is best illustrated by the M_G versus $G - W2$ and $G - W3$ plots in the Fig. 11, where the scatter of the subdwarfs and T dwarfs is markedly reduced. The 1.5–2 mag of spread in $G - W3$ colour for a given M_G for the whole spectral range through late M dwarfs, L dwarfs, and T dwarfs would likely make this the most useful diagnostic, though the increased errors and lack of depth of $W3$ magnitudes and consequent loss of subdwarfs limits the utility of this colour.

4.4 Spectral type–*Gaia* DR2 magnitude diagrams

In Fig. 12 we plot the absolute magnitudes in the G and G_{RP} bands versus published optical spectral types. For unresolved objects the observed spectral type is that of the brightest component, so it reflects the temperature of only that component. If it is an equal-mass system the observed spectral type is the approximate type of both components. For these passbands the subdwarfs tend to appear overluminous while the younger objects underluminous. The binaries are in general overluminous as the spectral type is the temperature of only one component, while the magnitude has a contribution from both components. The differences are not always consistent because the contributions of the secondaries vary. However, the G_{RP} magnitudes are more offset than the G magnitudes due to those estimates being the combined values instead of the component values. In light of our discussion in Section 4.2 about problems with G_{BP} and the higher signal to noise of G_{RP} , in future *Gaia* data releases it might well be appropriate to make comparisons using G_{RP} rather than G . We have also made similar plots comparing to the spectral types determined from the NIR colours (not shown) and the relations are similar to those shown, though with larger spreads.

4.5 Absolute magnitude relations

There have been many determinations of the relation between absolute magnitude and spectral types. For M, L, and T dwarfs this has been derived as a simple polynomial fit to a sample of classified objects with measured parallaxes and apparent magnitudes (e.g. for M, L, and T dwarfs see Dahn et al. 2002; Henry et al. 2004; Vrba et al. 2004; Dupuy & Liu 2012; Marocco et al. 2013). While the number of objects per spectral class bin was small and the relative error of the parallaxes was large, such a simple approach was justified. The *Gaia* LT dwarf sample is, especially for early L dwarfs, large and the relative error of the *Gaia* DR2 parallaxes are small so this approach is no longer sufficient.

The determination of an absolute magnitude calibration is not straight forward and there are a number of pitfalls:

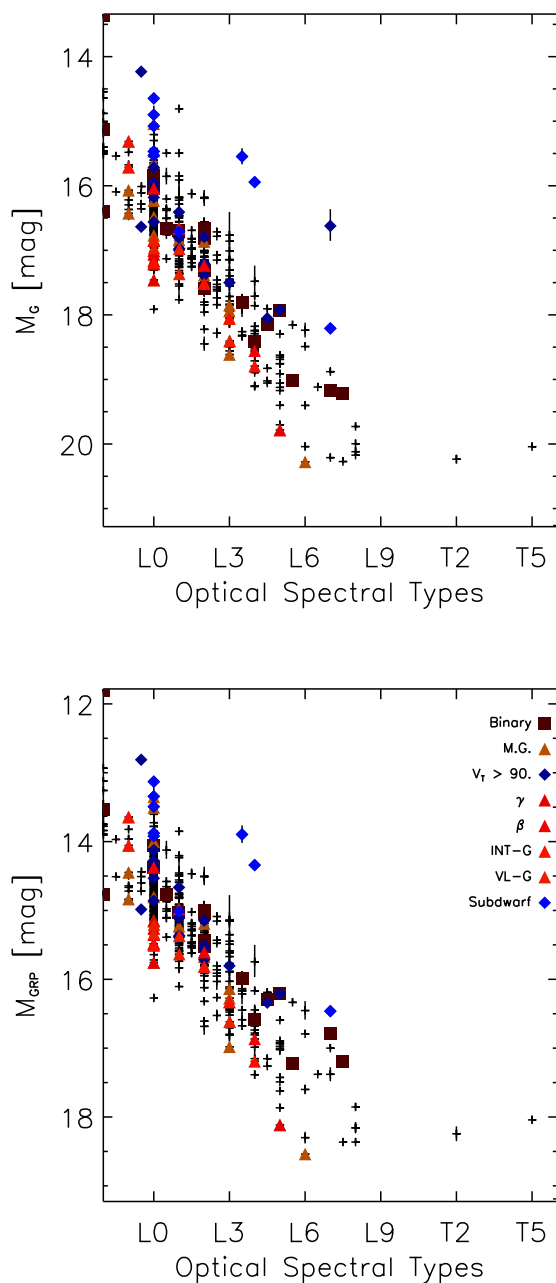
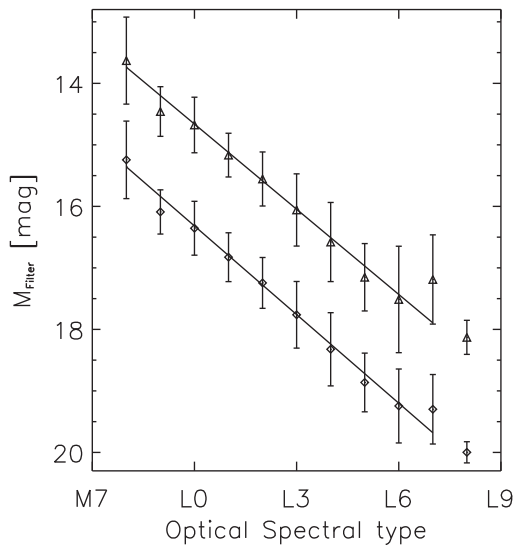


Figure 12. Absolute magnitude in G (top) and G_{RP} (bottom) passbands versus optical spectral types.

- (i) when using the parallax with assumed Gaussian uncertainties to determine the absolute magnitude the resulting uncertainties in magnitude are non-Gaussian (Lutz & Kelker 1973; Smith 2003; Bailer-Jones 2015; Luri et al. 2018);
- (ii) the use of a magnitude-limited sample leads to Malmquist-like biases;
- (iii) young and old objects within the same spectral class have absolute magnitudes that are systematically different, biasing the results;
- (iv) close unresolved binaries bias the calibration to brighter magnitudes;
- (v) there is no physical reason to assume that the absolute magnitude and spectral types are related by a smooth polynomial.

Table 7. Absolute G magnitude *Gaia* DR2 calibration.

SpT Opt	N	M_G (mag)	M_{R_p} (mag)
M8	16	15.24 ± 0.63	13.63 ± 0.71
M9	17	16.09 ± 0.36	14.46 ± 0.40
L0	234	16.36 ± 0.44	14.68 ± 0.45
L1	103	16.83 ± 0.40	15.17 ± 0.36
L2	68	17.24 ± 0.41	15.55 ± 0.44
L3	41	17.76 ± 0.54	16.06 ± 0.59
L4	26	18.32 ± 0.60	16.58 ± 0.64
L5	17	18.86 ± 0.48	17.15 ± 0.55
L6	6	19.25 ± 0.60	17.51 ± 0.87
L7	8	19.30 ± 0.56	17.19 ± 0.73
L8	4	20.00 ± 0.17	18.13 ± 0.28

**Figure 13.** Absolute G (triangles) and G_{RP} (diamonds) magnitudes versus optical spectral types. The points represent the medians as reported in Table 7, the lines are the straight line fit to observations of M8–L6 objects for the two passbands with parameters reported in Table 8.

Some of these problems can be alleviated by assuming an absolute magnitude versus colour relation (e.g. Bochanski, Hawley & West 2011), but the use of colour introduces other problems such as the inflection in colour at the L-T transition (Tinney, Burgasser & Kirkpatrick 2003).

For the *Gaia* DR2 passbands we find the absolute magnitudes as a function of optical spectral type for the bins where we have four or more objects, as presented in Table 7. The points in Fig. 13 are the inferred median absolute magnitudes per spectral type calculated taking into account that the uncertainties in the absolute magnitudes are neither Gaussian nor symmetric. The medians were obtained using a Bayesian hierarchical model assuming that within each spectral type bin there is a natural spread due to evolution and other effects (for example metallicity), and an additional scatter due to the observational uncertainties in the apparent magnitude and parallax. The comparison with the observations that yield the likelihood term is done in the space of parallaxes and apparent magnitudes. No distance estimation is involved and no smoothness constraint is enforced in the model.

As can be seen in Fig. 13 the relation between M8 and L6 is linear, which is true for the other passbands. The number of objects in the other passbands is lower and the apparent magnitude precision is

Table 8. Linear fits to absolute magnitude and spectral type for different passbands.

Absolute magnitude	N	a_λ (mag)	b_λ (mag)
Optical SpT			
M_G	477	-17.303 ± 0.568	0.480 ± 0.004
M_r	323	-11.159 ± 1.977	0.419 ± 0.033
M_i	380	-18.351 ± 0.771	0.489 ± 0.008
M_{R_p}	455	-17.663 ± 1.162	0.462 ± 0.016
M_z	356	-18.001 ± 1.436	0.463 ± 0.013
M_y	358	-17.957 ± 0.627	0.449 ± 0.003
M_J	475	-14.479 ± 0.408	0.373 ± 0.005
M_H	444	-11.304 ± 0.750	0.317 ± 0.010
M_{K_s}	442	-9.342 ± 0.568	0.282 ± 0.008
M_{W1}	438	-4.983 ± 1.036	0.216 ± 0.008
M_{W2}	435	-4.008 ± 0.955	0.198 ± 0.010
M_{W3}	422	-11.554 ± 0.878	0.292 ± 0.012
Infrared SpT			
M_G	319	-7.717 ± 0.979	0.347 ± 0.017
M_r	197	0.446 ± 2.305	0.257 ± 0.033
M_i	254	-10.941 ± 1.488	0.386 ± 0.016
M_{R_p}	300	-8.294 ± 1.545	0.331 ± 0.023
M_z	234	-10.109 ± 1.398	0.353 ± 0.022
M_y	239	-9.706 ± 1.776	0.334 ± 0.026
M_J	317	-8.001 ± 0.602	0.282 ± 0.009
M_H	313	-5.238 ± 1.460	0.232 ± 0.018
M_{K_s}	314	-4.367 ± 1.259	0.213 ± 0.019
M_{W1}	309	-0.232 ± 0.575	0.150 ± 0.008
M_{W2}	308	0.051 ± 0.868	0.142 ± 0.014
M_{W3}	299	-5.085 ± 0.948	0.202 ± 0.014

Parameters for equation (3): $M_\lambda = a_\lambda + b_\lambda \sim \text{SpT}$, valid in the range M8–L6. The top set of parameters applies when using optical spectral types and the lower set for infrared spectral types.

worse, so separate absolute magnitude estimates for each spectral bin is not warranted. Over this spectral range the error of a linear fit is smaller than the scatter, so to enable absolute magnitude estimates as a function of spectral type we made robust linear fits to all GUCDScat objects with published magnitudes of the form:

$$M_\lambda = a_\lambda + b_\lambda \text{SpT} \quad (3)$$

valid in the range SpT = 68 (M8)–76 (L6). In Table 8 we present the parameters for the linear fits for all passbands. We include for completeness the *Gaia* DR2 passbands, though we recommend using calibration in Table 7 for the most precise absolute magnitude estimates.

5 CONCLUSION

We have searched for known UCDs in the *Gaia* DR2 and found 695 with measured parallaxes, proper motions, and G magnitudes. We have matched this data set to publicly available large optical and infrared surveys, and produced a catalogue that we make available to the community and will use as a training set in the *Gaia* data processing chain of the UCDs work package. We have discovered 20 new multiple systems in our LT catalogue. We have examined a number of colour–magnitude diagrams finding significant main-sequence structure in the UCD region. We find the G_{BP} magnitude is not reliable for this sample and caution against using it for selection and interpretation.

We are currently using this sample to develop and refine procedures for a large-scale search of the full *Gaia* DR2 to discover

previously unknown UCDs. We expect there to be over 300 new LT dwarfs and there will be 1000s of new late M-type UCDs. We will catalogue and examine in an automatic way these new objects looking for fine structure in the spectrophotometric trends and find outlier objects that will indicate new physical processes or environments.

ACKNOWLEDGEMENTS

The authors thank the anonymous referee for a thorough review that increased the quality of this contribution. We thank Jonathan Gagné for useful discussions during the preparation of this manuscript. DB was supported by Spanish grant ESP2015-65712-C5-1-R; JCB by Proyecto FONDECYT postdoctorado 2018 nro. 3180716; FM by the NASA Postdoctoral Program at the Jet Propulsion Laboratory, administered by Universities Space Research Association under contract with NASA; JAC by Spanish grant AYA2016-79425-C3-2-P; HRAJ by the UK's Science and Technology Facilities Council grant number ST/M001008/1; RLS by a visiting professorship from the Leverhulme Trust (VP1-2015-063).

This publication makes use of reduction and data products from the Centre de Données astronomiques de Strasbourg (SIMBAD, cdsweb.u-strasbg.fr); the ESA *Gaia* mission (<http://sci.esa.int/gaia>) funded by national institutions participating in the *Gaia* Multilateral Agreement and in particular the support of ASI under contract I/058/10/0 (*Gaia* Mission - The Italian Participation to DPAC); the Panoramic Survey Telescope and Rapid Response System (Pan-STARRS, panstarrs.stsci.edu); the Sloan Digital Sky Survey (SDSS, www.sdss.org); the Two Micron All Sky Survey (2MASS, www.ipac.caltech.edu/2mass) and the Wide-field Infrared Survey Explorer (*WISE*, wise.ssl.berkeley.edu).

REFERENCES

- Allen P. R., Koerner D. W., Reid I. N., Trilling D. E., 2005, *ApJ*, 625, 385
 Allers K. N., Liu M. C., 2013, *ApJ*, 772, 79
 Alonso-Floriano F. J. et al., 2015, *A&A*, 577, A128
 Arenou F. et al., 2018, *A&A*, 616, A17
 Bailer-Jones C. A. L., 2015, *PASP*, 127, 994
 Baraffe I., Chabrier G., Barman T. S., Allard F., Hauschildt P. H., 2003, *A&A*, 402, 701
 Bardalez Gagliuffi D. C. et al., 2014, *ApJ*, 794, 143
 Bochanski J. J., Hawley S. L., West A. A., 2011, *AJ*, 141, 98
 Burgasser A. J., 2009, in Mamajek E. E., Soderblom D. R., Wyse R. F. G., eds, Proc. IAU Symp. Vol. 258, The Ages of Stars. Kluwer, Dordrecht, p. 317
 Burgasser A. J., McElwain M. W., 2006, *AJ*, 131, 1007
 Burgasser A. J., Tinney C. G., Cushing M. C., Saumon D., Marley M. S., Bennett C. S., Kirkpatrick J. D., 2008, *ApJ*, 689, L53
 Burgasser A. J., Dhital S., West A. A., 2009, *AJ*, 138, 1563
 Burrows A., Heng K., Nampaisarn T., 2011, *ApJ*, 736, 47
 Caballero J. A., 2009, *A&A*, 507, 251
 Caballero J. A., 2018, *Geosciences*, 8, 362
 Chabrier G., Baraffe I., Leconte J., Gallardo J., Barman T., 2009, in Stempels E., ed., AIP Conf. Proc. Vol. 1094, The Mass-Radius Relationship from Solar-type Stars to Terrestrial Planets: A Review. Am. Inst. Phys., New York, p. 102
 Chambers K. C. et al., 2016, preprint ([arXiv:1612.05560](https://arxiv.org/abs/1612.05560))
 Chauvin G., Lagrange A.-M., Dumas C., Zuckerman B., Mouillet D., Song I., Beuzit J.-L., Lowrance P., 2004, *A&A*, 425, L29
 Cruz K. L. et al., 2007, *AJ*, 133, 439
 Cruz K. L., Kirkpatrick J. D., Burgasser A. J., 2009, *AJ*, 137, 3345
 Dahn C. C. et al., 2002, *AJ*, 124, 1170
 Dahn C. C. et al., 2008, *ApJ*, 686, 548
 Day-Jones A. C. et al., 2011, *MNRAS*, 410, 705
 De Rosa R. J. et al., 2014, *MNRAS*, 445, 3694
 de Zeeuw P. T., Hoogerwerf R., de Bruijne J. H. J., Brown A. G. A., Blaauw A., 1999, *AJ*, 117, 354
 Deacon N. R. et al., 2014, *ApJ*, 792, 119
 Deacon N. R., Schlieder J. E., Murphy S. J., 2016, *MNRAS*, 457, 3191
 Deacon N. R. et al., 2017, *MNRAS*, 467, 1126
 Dhital S., West A. A., Stassun K. G., Bochanski J. J., 2010, *AJ*, 139, 2566
 Dhital S., West A. A., Stassun K. G., Schluns K. J., Massey A. P., 2015, *AJ*, 150, 57
 Dieterich S. B., Henry T. J., Jao W.-C., Winters J. G., Hosey A. D., Riedel A. R., Subasavage J. P., 2014, *AJ*, 147, 94
 Dittmann J. A., Irwin J. M., Charbonneau D., Berta-Thompson Z. K., 2014, *ApJ*, 784, 156
 Downes R. A. et al., 2004, *AJ*, 127, 2838
 Ducourant C., Teixeira R., Chauvin G., Daigne G., Le Campion J.-F., Song I., Zuckerman B., 2008, *A&A*, 477, L1
 Dupuy T. J., Liu M. C., 2012, *ApJS*, 201, 19
 Evans D. W. et al., 2018, *A&A*, 616, A4
 Faherty J. K. et al., 2012, *ApJ*, 752, 56
 Faherty J. K. et al., 2016, *ApJS*, 225, 10
 Filippazzo J. C., Rice E. L., Faherty J., Cruz K. L., Van Gordon M. M., Loofer D. L., 2015, *ApJ*, 810, 158
 Gagné J., Lafrenière D., Doyon R., Malo L., Artigau É., 2014, *ApJ*, 783, 121
 Gagné J., Lafrenière D., Doyon R., Malo L., Artigau É., 2015, *ApJ*, 798, 73
 Gagné J. et al., 2018, *ApJ*, 856, 23
 Gaia Collaboration, 2016, *A&A*, 595, A2
 Gaia Collaboration, 2018a, *A&A*, 616, A1
 Gaia Collaboration, 2018b, *A&A*, 616, A10
 Gálvez-Ortiz M. C., Solano E., Lodieu N., Aberasturi M., 2017, *MNRAS*, 466, 2983
 Gauza B., Béjar V. J. S., Pérez-Garrido A., Zapatero Osorio M. R., Lodieu N., Rebolo R., Pallé E., Nowak G., 2015, *ApJ*, 804, 96
 Gentile Fusillo N. P. et al., 2019, *MNRAS*, 482, 4570
 Haywood M., Jordi C., 2002, in Bienayme O., Turon C., eds, EAS Publ. Ser. Vol. 2, GAIA: A European Space Project. EDP Sciences, p. 199
 Henry T. J., Subasavage J. P., Brown M. A., Beaulieu T. D., Jao W.-C., Hambly N. C., 2004, *AJ*, 128, 2460
 Kirkpatrick J. D. et al., 2010, *ApJS*, 190, 100
 Kirkpatrick J. D. et al., 2012, *ApJ*, 753, 156
 Kirkpatrick J. D. et al., 2016, *ApJS*, 224, 36
 Kleinman S. J. et al., 2013, *ApJS*, 204, 5
 Lépine S., Gaidos E., 2011, *AJ*, 142, 138
 Lindegren L. et al., 2018, *A&A*, 616, A2
 Liu M. C., Dupuy T. J., Allers K. N., 2016, *ApJ*, 833, 96
 Lodieu N., Hambly N. C., Jameson R. F., Hodgkin S. T., 2008, *MNRAS*, 383, 1385
 Luhman K. L., 2013, *ApJ*, 767, L1
 Luhman K. L., Stauffer J. R., Mamajek E. E., 2005, *ApJ*, 628, L69
 Luri X. et al., 2018, *A&A*, 616, A9
 Lutz T. E., Kelker D. H., 1973, *PASP*, 85, 573
 Marocco F. et al., 2013, *AJ*, 146, 161
 Marocco F. et al., 2015, *MNRAS*, 449, 3651
 Marocco F. et al., 2017, *MNRAS*, 470, 4885
 Marsh K. A., Wright E. L., Kirkpatrick J. D., Gelino C. R., Cushing M. C., Griffith R. L., Skrutskie M. F., Eisenhardt P. R., 2013, *ApJ*, 762, 119
 Mason B. D., Wycoff G. L., Hartkopf W. I., Douglass G. G., Worley C. E., 2001, *AJ*, 122, 3466
 Montes D. et al., 2018, *MNRAS*, 479, 1332
 Murray D. N. et al., 2011, *MNRAS*, 414, 575
 Pecaut M. J., Mamajek E. E., 2013, *ApJS*, 208, 9
 Preibisch T., Zinnecker H., 1999, *AJ*, 117, 2381
 Reid I. N., Lewitew E., Allen P. R., Cruz K. L., Burgasser A. J., 2006, *AJ*, 132, 891
 Sahlmann J., Lazorenko P. F., Ségransan D., Martín E. L., Mayor M., Queloz D., Udry S., 2014, *A&A*, 565, A20

Sarro L. M., Berihuete A., Carrión C., Barrado D., Cruz P., Isasi Y., 2013, *A&A*, 550, A44
 Schmidt S. J., West A. A., Hawley S. L., Pineda J. S., 2010, *AJ*, 139, 1808
 Scholz R.-D., 2016, *A&A*, 587, A51
 Scholz R.-D., Bell C. P. M., 2018, *Res. Notes Am. Astron. Soc.*, 2, 33
 Scholz R.-D., McCaughrean M. J., Lodieu N., Kuhlbrodt B., 2003, *A&A*, 398, L29
 Secret N. J., Dudik R. P., Dorland B. N., Zacharias N., Makarov V., Fey A., Frouard J., Finch C., 2015, *ApJS*, 221, 12
 Skrutskie M. F. et al., 2006, *AJ*, 131, 1163
 Skrzypek N., Warren S. J., Faherty J. K., 2016, *A&A*, 589, A49
 Smart R. L., 2014, *Mem. Soc. Astron. Ital.*, 85, 649
 Smart R. L., Marocco F., Caballero J. A., Jones H. R. A., Barrado D., Beamín J. C., Pinfield D. J., Sarro L. M., 2017, *MNRAS*, 469, 401 (Paper 1)
 Smith H., 2003, *MNRAS*, 338, 891
 Smith L. C. et al., 2015, *MNRAS*, 454, 4476
 Smith L. C. et al., 2018, *MNRAS*, 474, 1826
 Soderblom D. R., 2010, *ARA&A*, 48, 581
 Tinney C. G., Burgasser A. J., Kirkpatrick J. D., 2003, *AJ*, 126, 975
 Vrba F. J. et al., 2004, *AJ*, 127, 2948

Wang Y. et al., 2014, *PASP*, 126, 15
 Wenger M. et al., 2000, *A&AS*, 143, 9
 West A. A. et al., 2011, *AJ*, 141, 97
 Wright E. L. et al., 2010, *AJ*, 140, 1868
 Zhang Z. H. et al., 2010, *MNRAS*, 404, 1817

SUPPORTING INFORMATION

Supplementary data are available at *MNRAS* online.

Table 3. Content of the GUCDScat with J1807+5015 as an example.

Please note: Oxford University Press is not responsible for the content or functionality of any supporting materials supplied by the authors. Any queries (other than missing material) should be directed to the corresponding author for the article.

This paper has been typeset from a $\text{\TeX}/\text{\LaTeX}$ file prepared by the author.